AN AMBIENT AIR SCANNING TUNNELING MICROSCOPE TO STUDY THE SURFACES OF THIN METAL FILMS

By

Joshua C. Wilson

A thesis submitted in partial fulfillment of the
requirements for the degree of

Bachelor of Science

Houghton University

May 2023

Signature of Author……
Department of Physics
May 10, 2023

……
Dr. Brandon Hoffman
Professor of Physics
Research Supervisor

……
Dr. Katrina Koehler
Assistant Professor of Physics

AN AMBIENT AIR SCANNING TUNNELING MICROSCOPE TO STUDY THE SURFACES OF THIN METAL FILMS

By

Joshua C. Wilson

Submitted to the Department of Physics
on May 10, 2023 in partial fulfillment of the
requirement for the degree of
Bachelor of Science

Abstract

An ambient–air scanning tunneling microscope (STM) is being built at Houghton University to study the crystal growth and transformation of thin metal films. The STM operates by maintaining a constant current between a piezoelectrically–controlled scanning probe and the thin metal film sample while recording the height of the probe relative to the sample stage. This current is produced when electrons from the sample quantum tunnel through the $\sim 10^{-10}$ m air gap to the probe, aided by a small bias voltage of ~-1 V applied to the sample. In order to achieve a tunneling gap of this size, the STM uses stepper motors to perform a rough approach of the probe to the sample. The STM is suspended on a dual-stage vibration isolation system which uses springs with eddy current damping to protect the STM from background noise. The STM is controlled by a user interface written in Processing and a Teensy 4.1 microcontroller via Arduino, along with a control circuit. The data collected by the STM are used to create an intensity plot that will act as an atomic resolution "image" of the film surface. All hardware, electronics, and programs have been completely and successfully tested.

Thesis Supervisor: Dr. Brandon Hoffman
Title: Professor of Physics

TABLE OF CONTENTS

TABLE OF FIGURES

Chapter 1

INTRODUCTION TO MICROSCOPY

1.1. Invention of the Electron Microscope

Around 400 B.C., the philosopher Democritus conceived the concept of the atom, which he called atomos, or indivisible. He theorized that the entire universe consisted of these particles, and scientists have spent the past two and a half millennia researching and developing this theory. Many different models of the atom were theorized, and properties of the atom were discovered, but still, no one had been able to see anything on the atomic level. This began to change in the 20th century with the introduction of electron microscopy.

Other microscopes had been invented prior to the 20th century, that focused visible light with a lens to magnify an image. However, in the 1920s, a German physicist named Hans Busch discovered [1,2] that a short coil can focus electrons using its magnetic field much like a lens can focus light. In addition, the focal length of this coil could be changed based on the magnitude of the current through the coil. Not long after Busch's discovery, two more Germans, physicist Ernst Ruska and electrical engineer Max Knoll, built the first electron microscope [3], shown in Figure 1, using two of these coils, giving it a magnification of 14.4x [1]. This low magnification results in rather low resolution images produced by the microscope, but the introduction of Louis de Broglie's theory of matter's wave properties [4,5] helped fix this problem. In simple terms, this theory states that since particles have momentum, they also have a wavelength inversely proportional to their momentum. Ruska and Knoll used his equations to determine that using an electron beam instead of light could result in a maximum resolution of 2.2 Å [1,6], or 0.22 nm, compared to visible light's maximum resolution of ~200 nm.

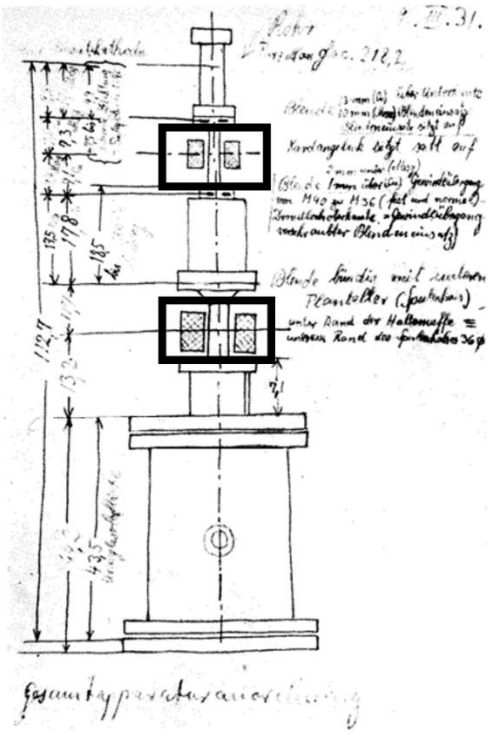

Figure 1. Ernst Ruska's drawing of the first electron microscope. The two sets of coils used in this design are shown in the outlined boxes. The first coil is called the objective magnetic lens and the second is called the projection lens [7]. Figure taken from Ref. [1].

1.2. Scanning Probe Microscopy

In the 1980s, a new type of microscopy was developed called scanning probe microscopy. Instead of shooting a beam of electrons at the surface to be imaged, these types of microscopes scan a small probe across the surface of the sample and use the interactions between the probe and surface to learn about the sample. These microscopes have the potential to reach the resolution limit discovered by Ruska and Knoll mentioned above. The first scanning probe microscope invented was the scanning tunneling microscope (STM) [8]. It works by allowing the probe to get within a few angstroms (Å) of the sample surface, and then uses principles of quantum mechanics to obtain a current between the probe and sample. This is known as a tunneling current because the electrons from the surface are tunneling, or passing through, the air gap to reach the scanning probe. This means that an STM can only be used to study samples with a conductive surface, since the surface is required to have a current pass through it. However, it also means that there is much less

risk of damaging the sample in the process of an STM scan, since the STM probe does not need to come in contact with the sample.

Two other examples of scanning probe microscopes are the atomic force microscope (AFM) and the scanning gate microscope (SGM). With an AFM [9], the probe is attached to a cantilever beam oscillating at a given frequency and allowed to come into contact with the sample surface. When coming in contact with the surface, the probe can be either attracted or repelled by the atomic force of the surface, changing the amplitude of the cantilever's oscillation. This change in oscillation is measured by reflecting a laser or particle beam off the cantilever and receiving it with a position-sensitive photodiode. This photodiode is capable of detecting the deflection angle of the beam and determining how much the amplitude of the cantilever was altered. In the first AFM, a conductive material was placed on the cantilever and an STM was used to generate a tunneling current to this material, which acted as the particle beam to measure the cantilever oscillation. An SGM [10] is very similar to an AFM and even uses the same setup and structure as an AFM. The only difference is that in an SGM, the probe is supplied with a voltage, meaning that when the probe contacts the surface, it repels electrons, providing information about how electrons are transported through the sample.

One advantage of AFM and SGM is that they are not limited to only studying conductors, since they do not rely on a current to obtain data. This means that they can be used to image insulators and conductors that have formed an oxidation layer on the top. Another advantage is that more recent forms of AFM and SGM are capable of imaging with higher resolution than an STM. Despite not having these advantages, the STM's primary advantage is its high spatial resolution given its simple design. The STM's design is simpler than that of the other microscopes, making it both easier and more cost-effective to build. While a more advanced AFM can achieve better resolution than an advanced STM, a simple STM design can reach higher resolutions than a simple AFM design. One of the very first STMs reached a lateral resolution of 5 Å, while the first AFM only reached a lateral resolution of 30 Å. Because of these advantages, the STM remains a popular choice for imaging crystal structures and surfaces.

1.3. The First Scanning Tunneling Microscope

The STM was made [8] in 1981 by German physicists Gerd Binnig and Heinrich Rohrer at the International Business Machines Corporation (IBM), with help from fellow IBM physicists Christoph Gerber and Edi Weibel. In the late 1970s, Binnig and Rohrer began researching how to perform spectroscopy on an area with a diameter less than 100 Å. The areas they were interested in were those of thin metal films. Lacking the tools to properly study them, they decided to combine the idea of vacuum tunneling with the process of scanning that was already present in other types of spectroscopy and microscopy. This combination led to what is known today as the STM. After Binnig and Rohrer applied for a patent [11] in January 1979, Gerber and Weibel were added to the research team to aid in the construction of the apparatus and testing of the vacuum tunneling. The main issue when trying to obtain a tunneling current is vibration isolation [8], which they reduced using a combination of different methods [12], as shown in Figure 2. The first method was to simply set the entire vacuum chamber on a bench made of stone, which was then placed on inflated rubber tubes; this isolated the chamber from building vibrations. The second method, used in conjunction with the first method, was to use static magnetic levitation by means of magnets and a superconducting lead bowl. This held the apparatus and prevented it from contacting any other surfaces. The bowl was insulated and cooled by liquid helium at a rate of roughly 20 L/h [8]. Lastly, a conductive sheet was placed between the magnets and lead bowl to provide eddy current damping. When the conductive sheet moved within the magnetic field produced by the magnets, currents were induced in the sheet that resulted in electromagnetic forces that opposed its motion.

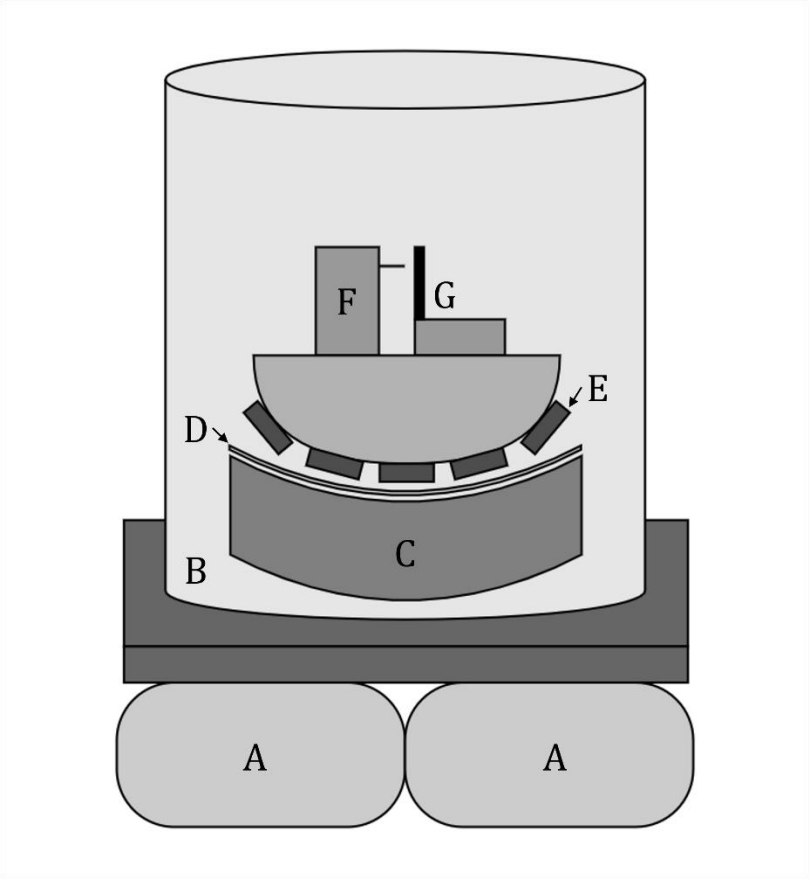

Figure 2. Diagram of the first STM. The inflated tubes (A) isolated the apparatus from building vibrations, while the vacuum chamber (B) housed the apparatus and maintained a pressure of 10^{-6} Torr. A lead bowl (C) was cooled to ~4.15 K by liquid He. Because the bowl is superconducting, it repels the magnets (E), causing the STM (F) and the sample holder (G) to levitate. The presence of the conductive sheet (D) results in eddy current damping to mitigate the STM's motion while levitating.

The scan was performed with the aid of two separate piezoelectrically-controlled systems, shown in Figure 3. The first system was the piezo drive and consisted of three separate piezoelectric materials, each of which controlled one direction of the scanning probe, as shown in Figure 4. This piezo drive system moved the probe in each direction through the use of 100 Hz driving signal waveforms of 1000 V pulses [11]. The other system consisted of a plate made of piezoelectric material, resting on three feet electrically isolated from one another. Each foot was free to glide around but could be electrostatically clamped down by applying a voltage to it. Combinations of clamping the feet and expanding or contracting

the material allowed the sample to be moved perpendicular to the probe and closer and farther from the probe.

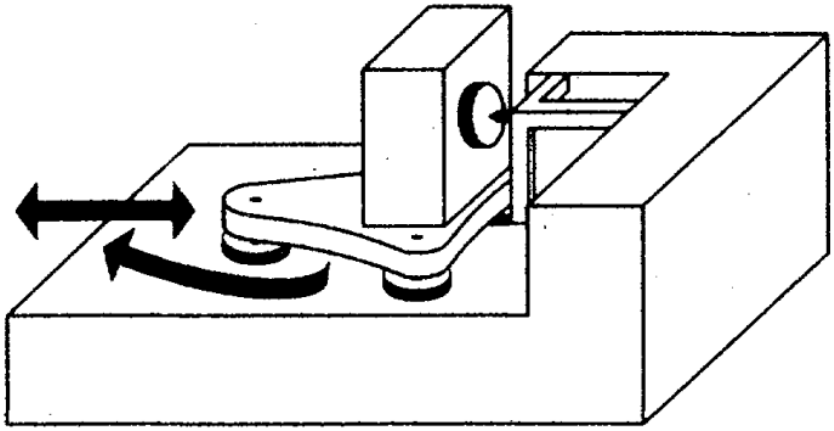

Figure 3. Diagram showing the piezo control for sample stage of the first STM. The sample was mounted on a triangular piezoelectric plate, which rests on three metal feet electrically isolated from one another. These feet could be electrostatically clamped down by applying a voltage to them, otherwise they were free to glide. The probe was brought close to the sample through combinations of expanding/contracting the piezo plate and clamping the feet. Figure taken from Ref [8].

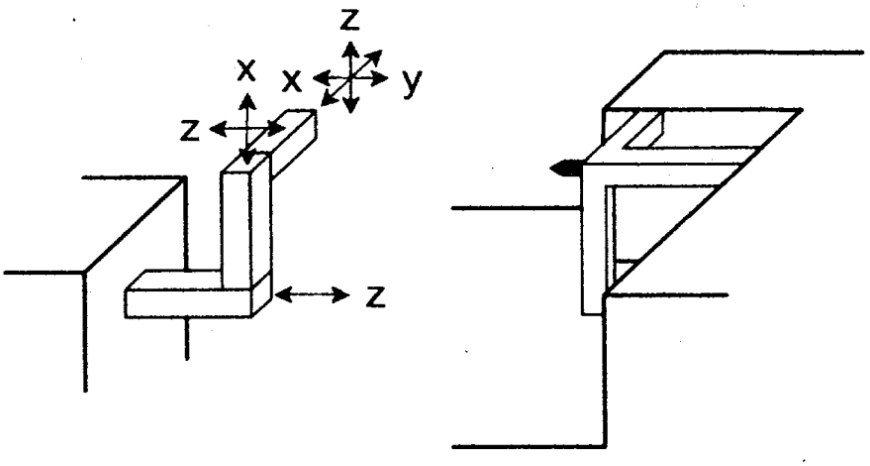

Figure 4. Diagrams showing the piezo control for the scanning probe of the first STM. The left diagram emphasizes the fact that each direction was controlled by a separate piezoelectric material. The diagram on the right shows how this method was applied in the actual design of the first STM. Figure taken from Ref [8].

With the chamber at roughly 10^{-6} Torr, the apparatus isolated from vibrations, and using a probe voltage of ~60 mV [12], the first exponential dependence of tunneling current on the tunneling gap was obtained. More experimentation was performed after this discovery to confirm the results of the last experiment, but this is generally considered the official creation of the STM.

1.4. Uses of the Scanning Tunneling Microscope

One outstanding use of the STM was the creation of the atomic force microscope. As stated in Section 1.2, the AFM measures the surface topography by shooting a particle beam at the cantilever beam; in the first AFM, an STM was used to provide this particle beam [9] by attaching a thin metal film to the back of the cantilever, so that the tunneling current became the particle beam. More common uses of scanning tunneling microscopy are the study of single crystal surfaces [13-17] and thin films [18-19].

1.4.1. Manipulation of a Surface

Scanning tunneling microscopes have been used to alter single crystal surfaces in a variety of ways. One example is a study in which small islands of copper were deposited onto a gold surface using an STM [14]. In order to accomplish this, copper was deposited onto the probe by holding it at a negative potential relative to a copper cation solution. The probe holding the copper was brought close to the sample; the copper is then able to bond to the surface of the sample by what was referred to as jump-to-contact, which is theorized to be a consequence of surface diffusion. When the probe was pulled away, the copper broke away from the probe, leaving a small cluster on the surface, as shown in Figure 5. These clusters were no more than 1 nm in height and had diameters, defined at half maximum height, between 3 and 4 nm. The researchers were able to place 400 clusters in a 20 by 20 grid with all clusters being equally sized, due to a constant deposition rate of copper onto the probe and onto the surface; it was also shown that clusters could be deposited in such a way that they were in a continuous line, touching side-by-side, to make a sort of deposited wire.

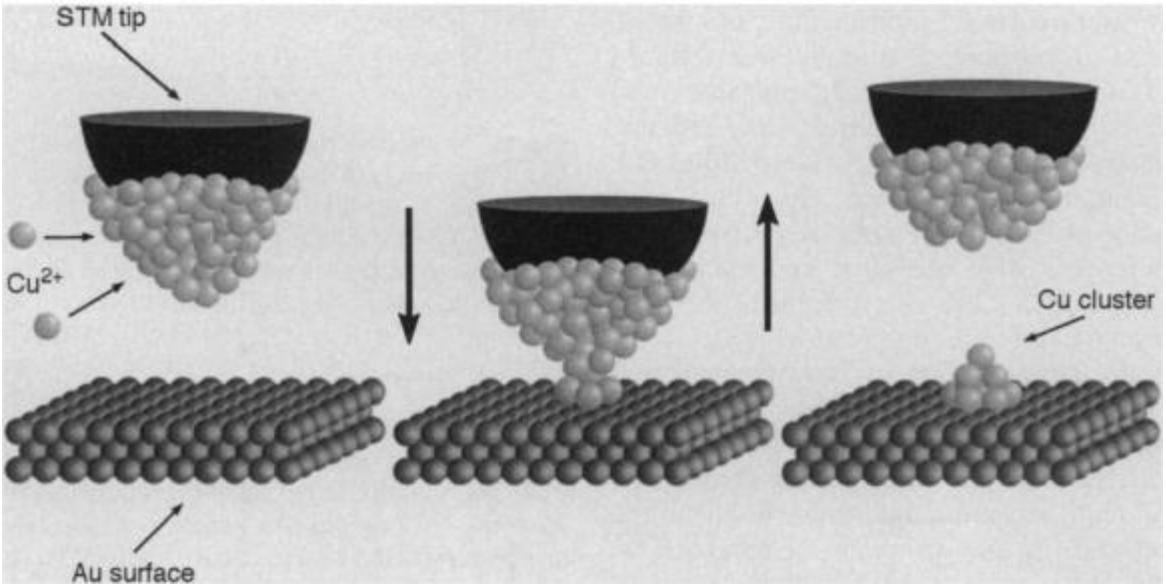

Figure 5. Diagram showing deposition of copper using an STM. This process is called jump-to-contact and occurs when the probe is brought near to the sample, so that the copper can jump to the sample and bond with it. When the probe is pulled away from the sample, the copper breaks away from the probe and remains on the sample. Figure taken from Ref [14].

In another study [15], an STM was used to alter single crystal surfaces in three ways: desorption of absorbed elements, the movement of molecules within the surface, and induction of chemical reactions within the surface. Each process was achieved by using the STM to excite molecules within the surface by electronic and vibrational excitation. Electronic excitation was achieved when an electron tunneled from the probe to an atom with energy equal to that of the resonant state level of an antibonding orbital. As a result, the antibonding orbital was temporarily filled, causing the atom to move to an excited state. The molecules were excited vibrationally through two methods: vibrational heating and resonant tunneling. Vibrational heating was achieved when holes that tunneled from the probe to the sample were inelastically scattered, and resonant tunneling was achieved when an electron tunneled through two barriers with an energy near that of a metastable state in the well between the barriers.

Desorption, molecular movement, and chemical reactions were controlled by the bias voltage applied to the sample, which in turn controlled the tunneling current and how much energy the atoms in the film receive. When the bias voltage was held at 60 mV,

enough energy was supplied to the atoms in the sample for them to react with one another, but not move around. For bias voltages in the range of 200–600 mV, the tunneling current supplied enough energy to the atoms for them to be able to move away from their bound locations in the film, but not enough to leave the sample. Finally, in the bias voltage range of 2–5 V, the atoms were supplied with enough energy for them to fully break their bonds and be desorbed from the surface.

1.4.2. Studying Crystal Properties

Scanning tunneling microscopy is useful for studying some properties of crystal samples, such as the formation of the crystal structure and its orientation, as well as reconstruction of the crystal surface and steps caused by cutting the crystal. Thin films are polycrystalline materials, meaning they are comprised of microscopic crystals. These crystals are typically called grains because relative to the size of the film, they are small. A crystal is a 3-D lattice, which is made by placing the same set of atoms at each lattice point. One example of a crystal is a face-centered cubic (FCC) crystal; this crystal is comprised of sets of four atoms placed around each lattice point. One atom is on the lattice point and the others surround this atom at positions $\frac{a}{2}\hat{\imath} + \frac{a}{2}\hat{\jmath}$, $\frac{a}{2}\hat{\imath} + \frac{a}{2}\hat{k}$, and $\frac{a}{2}\hat{\jmath} + \frac{a}{2}\hat{k}$, as shown in Figure 6, where a is the length of the lattice vector. The lattice vector is a vector that points from one lattice point to another adjacent lattice point. Another type of lattice structure is the diamond cubic structure, which is formed by carbon. This structure is very similar to that of the FCC structure, but instead of four atoms at each lattice point, this structure has four pairs of atoms at each lattice point, resulting in a total of 8, as shown in Figure 7. In each pair, one is the same as that in the FCC structure, and the other is located at $\frac{a}{4}\hat{\imath} + \frac{a}{4}\hat{\jmath} + \frac{a}{4}\hat{k}$ relative to the FCC atom. As a result of this similarity, the diamond cubic structure is commonly referred to as an FCC crystal with a two-atom basis.

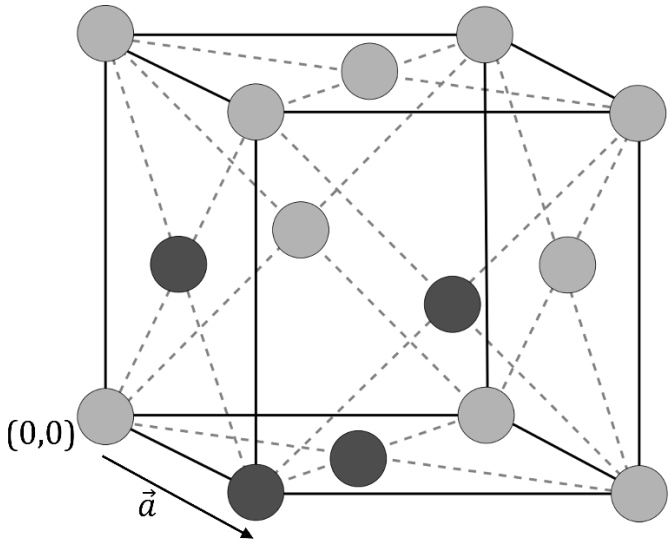

Figure 6. An example of a face-centered cubic (FCC) crystal structure. Each corner of the cube represents a lattice point, and the length of a side of the cube is the length of the lattice vector $\vec{a}$. At each lattice point there are four atoms (those labeled with the darker shade of grey): the atom on the lattice point and then the three atoms on the three adjacent faces of the cube.

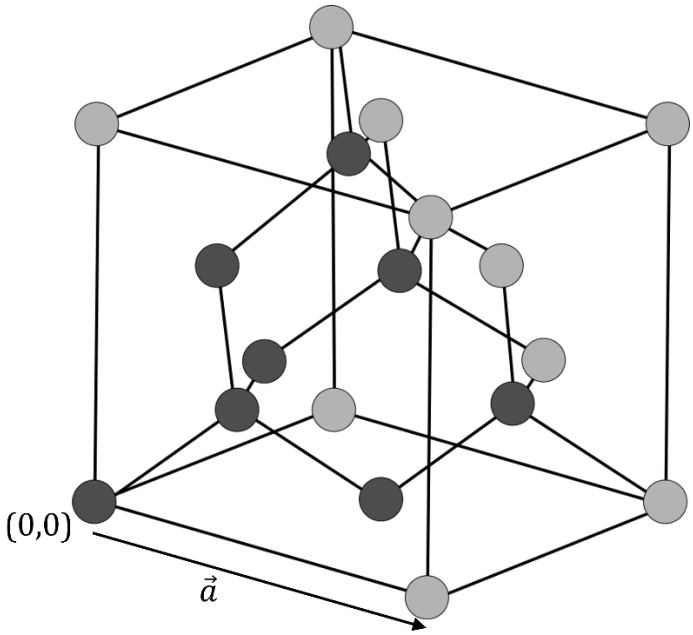

Figure 7. An example of a diamond cubic lattice structure. Comparing this structure to that of the FCC lattice, shown in Figure 6, shows that they are very similar to one another, but this structure has four pairs of atoms at each lattice point as opposed to four single atoms (shown in a darker shade of grey), giving it a two-atom basis. As with the FCC structure, each corner of the cube is a lattice and the length of a side of the cube is equal to the length of the lattice vector $\vec{a}$.

The grain orientations in thin films are given by their Miller indices. Miller indices give the film's normal vector in terms of a crystal grain's lattice vectors. This is shown in Figure 8 for the three most common Miller indices: (100), (110) and (111).

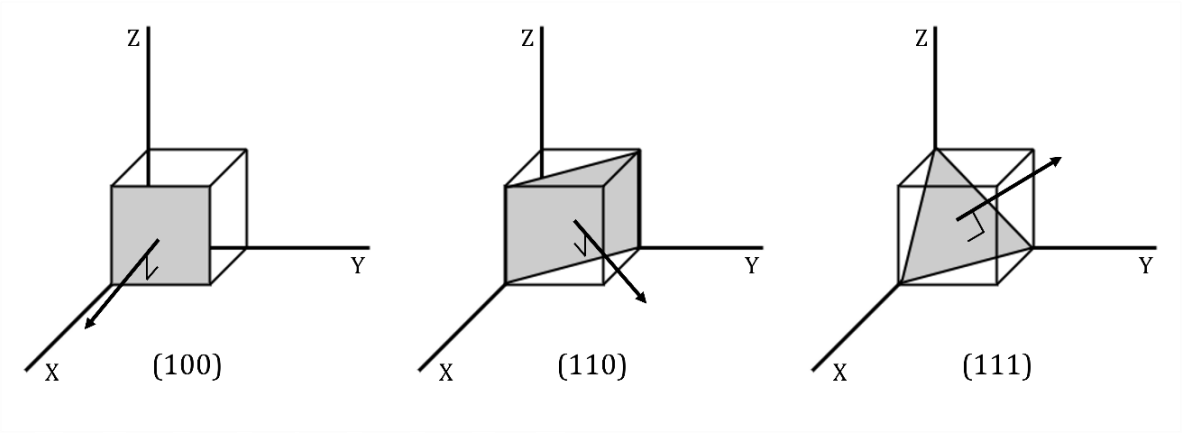

Figure 8. Depiction of the (100), (110) and (111) Miller indices. In each graph, the shaded area represents the plane that the grain's normal vector is perpendicular to. From this it can also be seen how the normal vector can be written in terms of the lattice vectors; for example, (111) is written as $a\hat{\imath} + a\hat{\jmath} + a\hat{k}$, where a is the length of a lattice vector.

At the surface of a crystal, the top few layers of atoms have an imbalance of forces on them, causing them to reorient their structure in order to balance the forces, which is known as surface reconstruction. As mentioned above, a crystal has a system of repeating patterns of atoms; an unreconstructed crystal has a pattern of 1x1, meaning that the structure can be broken up into 1x1 squares of the same repeating pattern. After the surface is reconstructed, this pattern is altered; some examples of a new pattern could be 2x1, 4x2, or even 7x7, as shown in Figure 9.

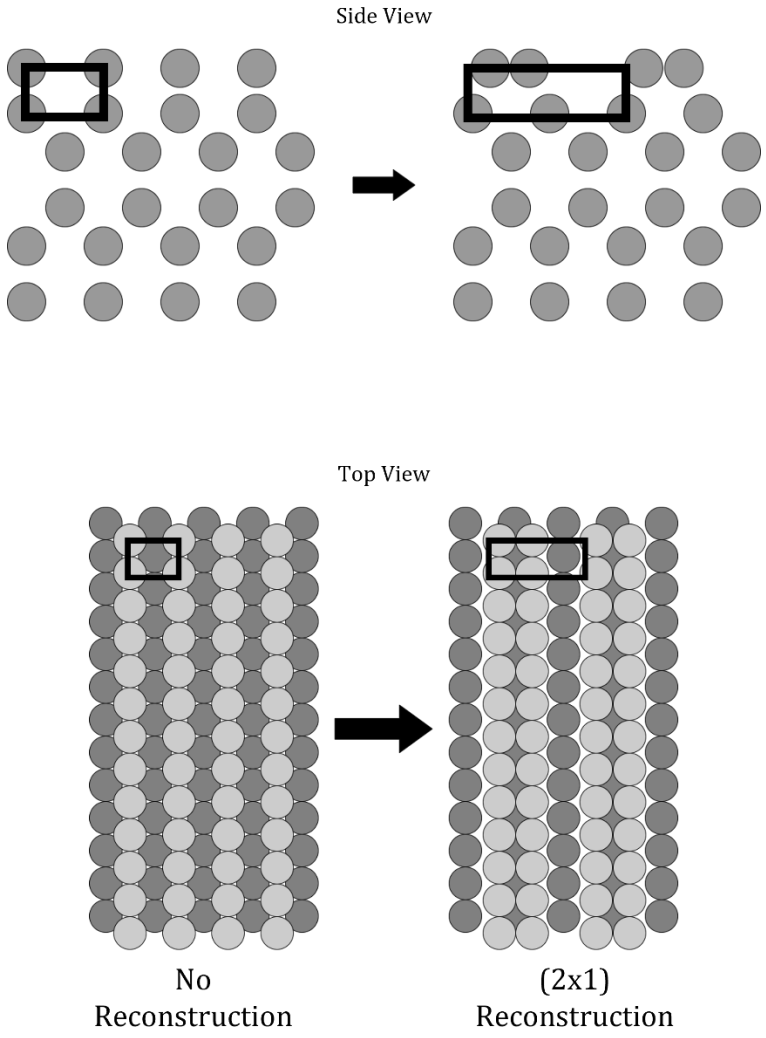

Figure 9. Side– and top–view of a film undergoing (2x1) reconstruction. After the film is cut, the atoms in the top layer are left in a higher energy state, as shown in the left side. In this reconstruction, the atoms bond with those next to them in order to reduce their energy state, as shown in the right side.

In addition to reconstruction, steps are another thing that occurs at the surface of a crystal. If a crystal is cut at an angle relative to its lattice vector, the distance between steps is an indication of how large of an angle it was cut at. Both the steps and the reconstruction of the crystal surface can also be altered by the temperature of the crystal, which can be studied using STM.

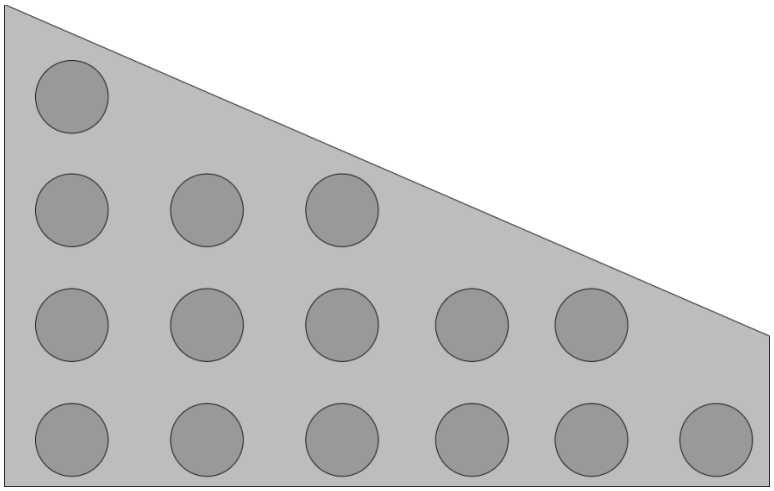

Figure 10. Diagram showing steps in a cut crystal. When a crystal is cut at an angle relative to its lattice vectors, steps in the lattice will occur. In this example, every two atoms, the lattice goes down a step as a result of being cut.

In a study [16] by Binnig and Rohrer, an STM was used to image the surfaces of a few different samples. With each sample, their STM measured distances below 10 Å, resulting in images with atomic resolution. For their Au(110) sample, the surface was imaged at both room temperature and at 300 °C; at room temperature, the sample surface was mostly smooth, with only a few steps, but at the higher temperature, the surface had many more steps, indicating an increase in surface roughness. It was shown that surface reconstruction on this film may not disappear until ~400 °C, so it was speculated that this is why the surface became rougher at only 300 °C. STM imaging of a Si(111) surface, known to have a 7x7 reconstruction pattern, revealed instead a pattern of equilateral triangles. By using the STM, they were able to infer potential contaminants in the reconstruction process, since the Si did not have its normal pattern.

In another study [18] by C. Polop et. al., an STM was used to study crystal structure formation as a function of film thickness. Silver was deposited onto a silicon substrate at a set temperature and deposition rate. During this growth process, the deposition was periodically paused so that an STM image of the film could be taken. With each image, measurements were focused on the islands of silver on the silicon substrate; an island is a cluster of silver not in contact with any other cluster of silver. Through these

measurements, information was gathered about the change in island density as a function of film thickness. The researchers were also able to see the development of the film's (111) grain orientation in the islands as they formed. The islands do not necessarily start growing with a (111) orientation, but as they grow larger and combine with each other, the (111) orientation begins to form. With each film thickness that was imaged, this change in the structure development could be seen. The final area that was studied was the effect of annealing temperature; annealing is the process of heating a film up after it is grown and then letting it cool, in order to relieve stress on the grain structure and to make the surface of the film smoother. In this study it was shown that as the annealing temperature was increased, the more the grain structure changed in a way to make the film smoother. For two films, each grown at 300 K, but one annealed at 400 K and one annealed at 500 K, the grains of each film experienced a growth in size. However, while the surface of the film annealed at 400 K becomes rougher, the surface of the film annealed at 500 K actually became smoother. This is because at that higher temperature, the grains were able to reorient themselves in a way that decreased the roughness of their structure.

An ambient-air STM was used in a study [19] to determine how film deposition, annealing temperatures, and annealing times would affect the structure of an indium tin oxide (ITO) thin film. In this study an STM was used to image three different sets of films in three different experiments. In each experiment four 498 nm × 498 nm images were taken of each film using a 1.4 V sample bias with a constant 0.03 nA tunneling current.

In the first experiment, four films deposited at 40 °C, 200 °C, 325 °C, and 400 °C, respectively, were imaged directly after deposition, shown in Figure 11. This experiment found that films deposited at the two higher temperatures were flatter and more uniform than those deposited at the two lower temperatures. It was also noted that at higher deposition temperatures, the grains in the film were smaller and more defined ($\sim 5 \pm 1$ nm) than at lower temperatures (~10 nm).

In the second experiment the films were deposited at the same temperatures as the first experiment and then annealed in air for 1 h at 300 °C. Each film was then compared to itself by looking at its properties from before and after annealing. After annealing, the 325 °C film

did not change substantially and the 400 °C film showed only a surface that was slightly rougher than before. The 200 °C and 40 °C films experienced more changes than the other two; the roughness of the film's surface decreased for both films, and two distinct grain sizes (~5 nm and ~40 nm) became noticeable in the 40 °C film.

In the final experiment, the STM was used to determine the effect of annealing time on the film structure. Each film was deposited at 325 °C, and then annealed in air at 300 °C for 0 h, 1 h, 2 h, and 3 h. The films annealed for 0 h and 1 h had the same topographical features as their corresponding films from the first two experiments. The films annealed for 2 h and 3 h, on the other hand, experienced topographical changes. These two films exhibited some sort of breaking pattern caused by the annealing process. They were no longer flat but contained numerous valleys of nanometer depth along the surface, where the film was more likely to break.

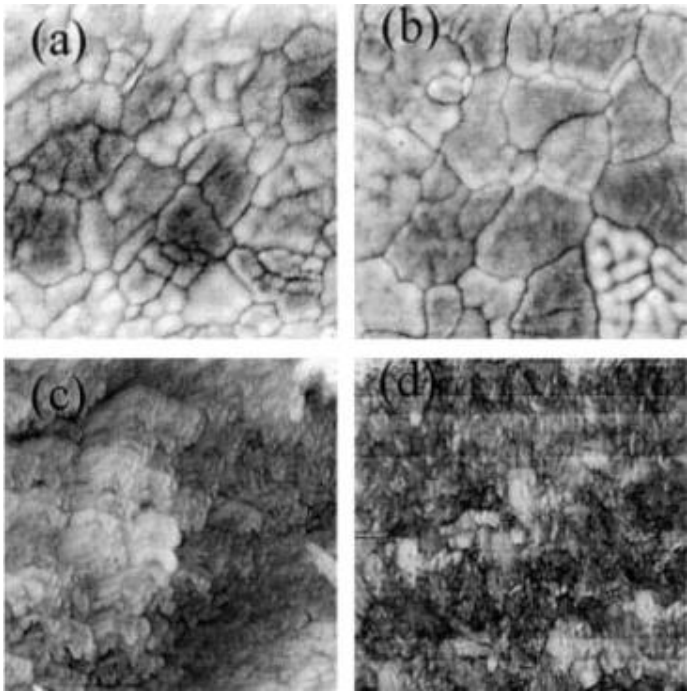

Figure 11. Ambient–air STM images of indium tin oxide (ITO) thin films. These films were deposited at (a) 400 °C, (b) 325 °C, (c) 200 °C, and (d) 40 °C. Films (a) and (b) have smaller and more defined grains than films (c) and (d). The surfaces of (a) and (b) are also more uniform than (c) and (d). Each image is 498 nm x 498 nm in size. Image taken from Ref [19].

1.5. The Houghton University Scanning Tunneling Microscope

These are the types of thin metal film research that we wish to continue at Houghton University. Under the supervision of Dr. Brandon Hoffman, a thin metal film research lab is under construction. Other projects in this lab include a physical vapor deposition (PVD) chamber [20], an x–ray diffractometer (XRD) [21], and a phase-shifting laser interferometer [22]. The PVD chamber will be used to produce the thin metal films to be studied; it operates by applying a voltage to a filament that accelerates electrons toward a graphite crucible holding the metal to be deposited. The electrons heat up the metal, causing it to evaporate out of the crucible and deposit onto a substrate. The interferometer is used to study the surface topography of thin metal films by looking at the interference pattern of two laser beams: one that reflects of a reference mirror and one that reflects off the sample. The XRD is used to study the film's crystal structure by bombarding the sample with x-rays and then measuring the intensity of the deflected beams.

The STM will be used similarly to the XRD and interferometer; it will be used to study a few key things about the films made by the PVD chamber, similar to those from the studies discussed above: the effect of temperature on the grain structure, how the crystal structure changes with a gradient film vs. a flat film, how the grains develop over the growth process, etc. The goal of this STM is to be both easy and cost-effective to build, as well as easy to operate. While the STMs in the above studies were operated under ultra-high vacuum, the STM at Houghton University will be operated at atmospheric pressures. However, similarly to past STMs, the probe on this STM will be controlled using a piezo buzzer, a type of piezoelectric material that deforms when a voltage is applied to it. This piezo buzzer can be modified to allow the probe to be moved in all three dimensions. The STM will also contain vibration damping similar to other STMs; system control and data handling will be performed using a microprocessor along with digital–to–analog converters and an analog–to–digital converter.

Chapter 2

THEORY OF SCANNING TUNNELING MICROSCOPY

2.1. Quantum Theory

The operation of a scanning tunneling microscope relies heavily on principles of quantum mechanics and the current that exists between the probe and the sample is a direct result of these principles.

2.1.1. Wave–Particle Duality

A main principle in quantum mechanics is wave–particle duality, which describes particles, such as electrons, photons, etc., as having the properties of both particles and waves. This theory was developed through a number of experiments, most notably Thomas Young's double-slit experiment [23], Max Plank's work on blackbody radiation [24], and Albert Einstein's work on the photoelectric effect [25,26]. However, one of the most notable advancements in this theory was Louis de Broglie's discovery of the phase wave [4,5]. De Broglie derived the equation

$$\lambda = \frac{h}{p}, \tag{1}$$

stating that the wavelength of a particle, λ, is inversely proportional to its momentum, p, by a factor of Planck's constant, h. This formula was derived by combining Einstein's equation

$$E = mc^2 , \tag{2}$$

relating the energy of a particle, E, to its mass, m, and the speed of light, c, and Planck's formula

$$E = h\nu , \tag{3}$$

relating the energy of a particle to its frequency, ν. This equation was used to propose the theory that all matter has a wavelength associated with it since all matter has some amount of momentum. Thus electrons and other particles might demonstrate wave–like properties.

This theory was shown to be true in Claus Jönsson's double–slit experiment [27]. In this experiment, an electron beam was shot at a set of thin slits, so that they would pass through the slits one–by–one. When the electrons hit the target after the slits, they were grouped up in clusters as shown in Figure 12. Claus Jönsson's double–slit experiment

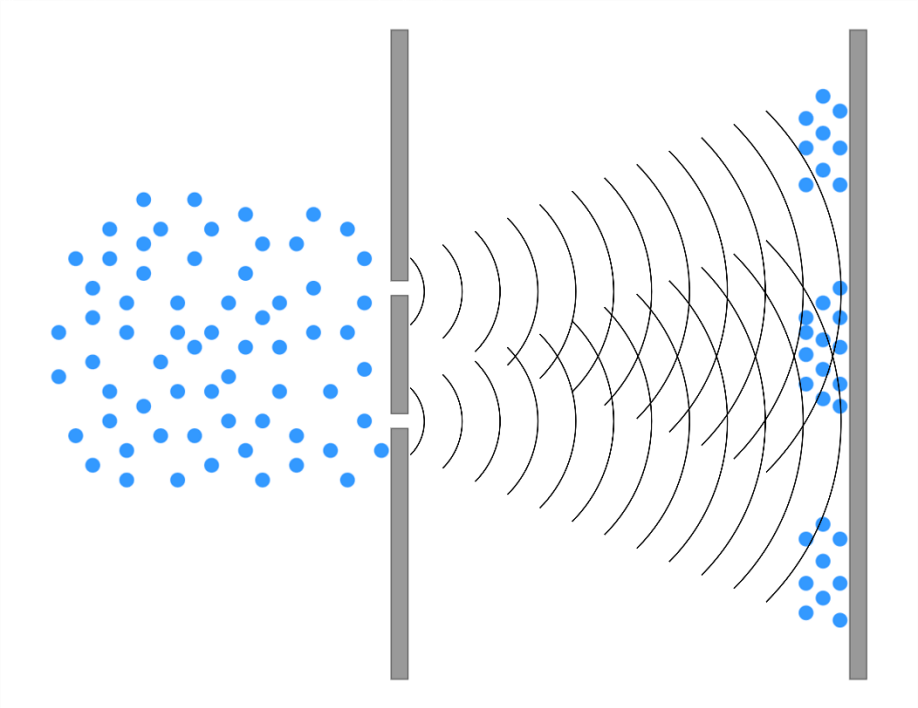

Figure 12. Claus Jönsson's double–slit experiment. An electron beam is shot at a set of thin slits and detected by a position-sensitive sensor behind the slits. The electrons were caught in what resembled a wave interference pattern.

These clusters resembled constructive and destructive wave interference patterns, with the electron clusters representing where the wave peaks and dips lined up. It was this result that showed that electrons do have wave–like properties in addition to those of particles, supporting de Broglie's theory.

2.1.2. Schrödinger's Equation

In 1926, Austrian physicist Erwin Schrödinger published an equation that relates an electron's wavefunction to its energy. This is what we know now as the Schrödinger equation and in its most simple form is written as

$$\hat{H}\Psi(x) = E\Psi(x)\,, \tag{4}$$

where $\Psi(x)$ is the wavefunction, E is the particle' and $\hat{H}$ is the Hamiltonian operator. In one dimension this equation expands to

$$\frac{-\hbar^2}{2m}\frac{d^2\Psi(x)}{dx^2} + V\Psi(x) = E\Psi(x)\,, \tag{5}$$

where ħ is the reduced Planck's constant, V is the potential energy of the particle, and x is the displacement of the particle. The wavefunction, $\Psi(x)$, is a probability amplitude for the particle and is the probability of finding the particle in the region. It is this idea of a particle as a probability wave that gives rise to the theory of quantum tunneling. Classically, if a particle has an energy lower than that of a potential barrier, it cannot be found on the other side of the barrier. Quantum mechanically, however, there is a finite probability that the particle can be found on the other side of the barrier, which is the concept behind the current between an STM probe and a sample.

2.2. Quantum Tunneling and Tunneling Current

The potential energy barrier in the STM is the air gap between the probe and the sample. A negative bias voltage will be applied to the sample relative to the tip so that the electrons in the sample will have higher potential energy than those in the tip. The potential energy barrier between the probe and sample is shown in Figure 13. Schrödinger's equation can be written for each region in Figure 13 using what we know about the potential energy in each region.

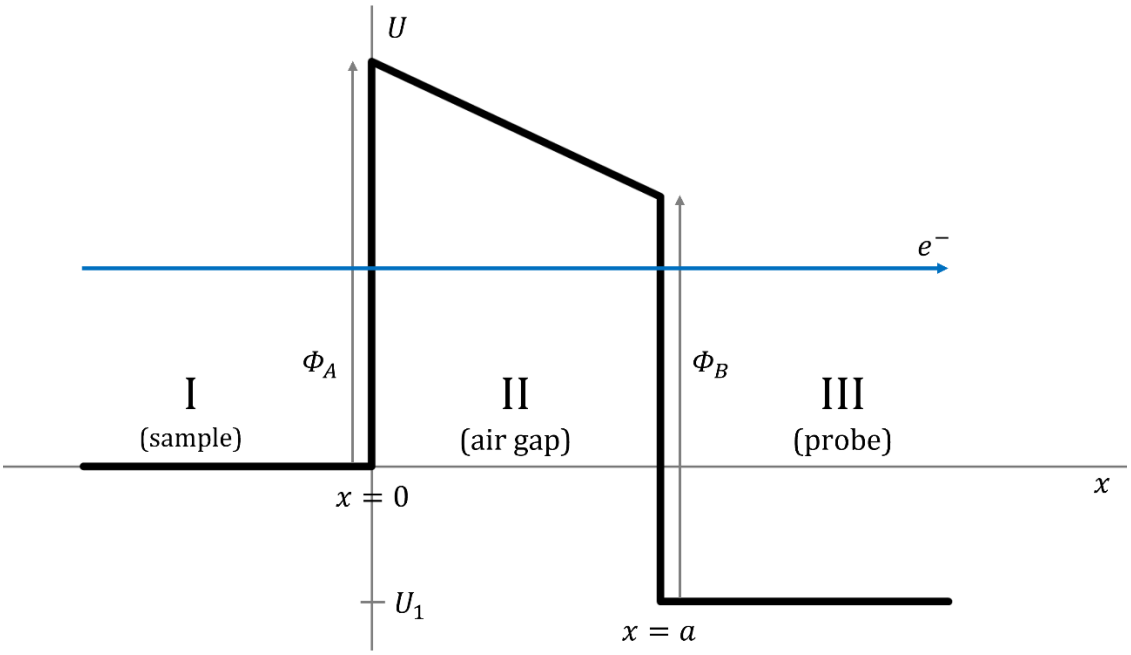

Figure 13. Potential energy vs. position graph of potential energy barrier for STM. The arrow labeled e^- represents the electron moving through the barrier. The region labelled I represents the sample and has a potential energy of 0, the region labelled II represents the potential energy barrier and has a potential energy as a function of x from $x = 0$ (the sample surface) to $x = a$ (the end of the probe), and the region labelled III represents the probe, which has a bias voltage of V_1. Φ_A and Φ_B represent the work functions of the sample and tip, respectively. The Fermi level is the highest probable energy state that an electron can exist at within a substance; in other words, it is improbable for an electron to exist above the Fermi level. For the sample side of the barrier the Fermi level is at 0 V, and for the probe side of the barrier the Fermi level is at U_1, because it is experiencing a bias voltage which shifts its Fermi level. Only electrons with energies between these two Fermi energies are free to tunnel through the barrier from region I to region III.

In region I, the potential energy is equal to zero, since it does not have any sort of bias, so therefore, Schrödinger's equation becomes

$$-\frac{\hbar^2}{2m}\frac{d^2\Psi(x)}{dx^2} = E\Psi(x)\,, \tag{6}$$

the solution to which is

$$\Psi_I(x) = Ae^{i\frac{p_1}{\hbar}x} + Be^{-i\frac{p_1}{\hbar}x}\,, \tag{7}$$

where A and B are constants, i is $\sqrt{-1}$, and p_1 is given by

$$p_1 = \sqrt{2mE}\,. \tag{8}$$

Region III is similar to region I in that it has a constant potential energy U_1, so the Schrödinger equation becomes

$$-\frac{\hbar^2}{2m}\frac{d^2\Psi(x)}{dx^2} = (E - U_1)\Psi(x)\,, \tag{9}$$

which has the solution

$$\Psi_{III}(x) = Fe^{i\frac{p_3}{\hbar}x} + Ge^{-i\frac{p_3}{\hbar}x}\,, \tag{10}$$

where F and G are constants and p_3 is given by

$$p_3 = \sqrt{2m(E - U_1)}\,. \tag{11}$$

In this equation, the F term represents movement to the left and the G term represents movement to the right. However, since this region is after the potential energy barrier, any waves moving to the left are non-existent or negligible, so we can say that $G = 0$.

Unlike regions I and III, the potential energy in region II is a function of x. Using the slope-intercept form of a linear equation, the potential energy is given by

$$U(x) = \frac{(\Delta\Phi + U_1)}{a}x + \Phi_A\,, \tag{12}$$

where

$$\Delta\Phi = \Phi_B - \Phi_A\,, \tag{13}$$

with Φ_A and Φ_B being the work functions of the sample and tip, respectively, and a being the width of the potential energy barrier. This makes the solution to the wavefunction in region II more complicated. However, it can be approximated by using what is known as the Wentzel, Kramers and Brillouin (WKB) approximation [28]. To start, the Schrödinger equation for region II is written as

$$\frac{d^2\Psi(x)}{dx^2} = -\frac{p_2(x)}{\hbar^2}\Psi(x)\,, \tag{14}$$

where

$$p_2(x) = \sqrt{2m[E - U(x)]}\,. \tag{15}$$

Since *U(x)* is greater than E in region II, $p_2(x)$ is imaginary. The next step in the WKB approximation is to write the wavefunction as

$$\Psi(x) = e^{\frac{i}{\hbar}Q}\,. \tag{16}$$

If we make this substitution into the Schrödinger equation for this region and take the second derivative the equation becomes

$$\frac{i}{\hbar}Q'' - \frac{1}{\hbar^2}(Q')^2 = -\frac{p_2(x)^2}{\hbar^2}\,. \tag{17}$$

Multiplying this equation by $\hbar^2$ gives

$$i\hbar Q'' - (Q')^2 = -p_2(x)^2\,. \tag{18}$$

In order to solve for Q, we must say that ħ is the variable in the equation and that $\hbar \ll 1$. Q can then be expanded around ħ, and since it is small, only the first two powers of the expansion are kept:

$$Q = Q_o + \hbar Q_1\,. \tag{19}$$

Making this substitution in the wavefunction equation gives

$$i\hbar {Q_o}'' + i\hbar^2 {Q_1}'' - {Q_o}'^2 - \hbar^2 {Q_1}'^2 - 2\hbar Q_o' Q_1' = -p_2(x)^2\,. \tag{20}$$

Since only the first two powers of ħ are considered, the terms with $\hbar^2$ can be removed from the equation, then it can be separated into two equations based on the powers of ħ:

$$Q_0' = \pm p_2(x) \tag{21}$$

$$i{Q_o}'' = \pm 2Q_0' Q_1'\,. \tag{22}$$

Solving the first equation gives

$$Q_o = \pm \int p_2(x)\,dx\,. \tag{23}$$

The second equation can be solved by solving it for ${Q_1}'$ and substituting the definition of ${Q_o}'$ into it:

$$Q_1{}' = \frac{i}{2}\frac{p_2(x)'}{p_2(x)} \tag{24}$$

$$Q_1{}' = \frac{i}{2}[\ln p_2(x)]' \tag{25}$$

$$Q_1 = \frac{i}{2}\ln p_2(x) + C\,. \tag{26}$$

Using these results, the equation for the wavefunction becomes

$$\Psi(x) = e^{\pm\frac{i}{\hbar}\int p_2(x)dx} e^{i\left[\frac{i}{2}\ln p_2(x)+C\right]}, \tag{27}$$

and with some simplification it becomes

$$\Psi(x) = C_1\frac{1}{\sqrt{p_2(x)}} e^{\pm\frac{i}{\hbar}\int p_2(x)dx}\,. \tag{28}$$

Since both C_1 and $\sqrt{p_2(x)}$ are imaginary, they can be written as $iC_{\pm}$ and $i\sqrt{|p_2(x)|}$, respectively. Using these substitutions, the wavefunction equation is written as

$$\Psi_{II}(x) = \frac{C}{\sqrt{|p_2(x)|}} e^{\phi(x)} + \frac{D}{\sqrt{|p_2(x)|}} e^{-\phi(x)}, \tag{29}$$

where

$$\phi(x) = \frac{1}{\hbar}\int_0^x |p_2(x)|dx \tag{30}$$

and the constants C_+ and C_- have been replaced with C and D. The constants for the wavefunction equations can be solved for by looking at the boundary conditions. At the boundaries $x = 0$ and $x = a$, the wavefunctions for inside and outside the barrier are equal, and as a result the derivatives of the wavefunctions are also equal, giving the following boundary condition equations:

$$\Psi_I(x)|_{x=0} = \Psi_{II}(x)|_{x=0} \tag{31}$$

$$\left.\frac{d\Psi_I(x)}{dx}\right|_{x=0} = \left.\frac{d\Psi_{II}(x)}{dx}\right|_{x=0} \tag{32}$$

$$\Psi_{II}(x)|_{x=a} = \Psi_{III}(x)|_{x=a} \tag{33}$$

$$\left.\frac{d\Psi_{II}(x)}{dx}\right|_{x=a} = \left.\frac{d\Psi_{III}(x)}{dx}\right|_{x=a}. \tag{34}$$

Taking the derivatives and evaluating at $x = 0$ and $x = a$ gives:

$$A + B = \frac{C}{\sqrt{|p_2(0)|}} + \frac{D}{\sqrt{|p_2(0)|}} \tag{35}$$

$$ip_1A - ip_1B = \sqrt{|p_2(0)|}(C - D) \tag{36}$$

$$Fe^{i\frac{p_3}{\hbar}a} = \frac{C}{\sqrt{|p_2(a)|}}e^{\phi(a)} + \frac{D}{\sqrt{|p_2(a)|}}e^{-\phi(a)} \tag{37}$$

$$ip_3Fe^{ik_3a} = \sqrt{|p_2(a)|}\left[Ce^{\phi(a)} - De^{-\phi(a)}\right]. \tag{38}$$

There are five constants to solve for and only four equations to use, so in order to make this possible each equation is divided by A, giving four unknowns instead of five: $\frac{B}{A}$, $\frac{C}{A}$, $\frac{D}{A}$, and $\frac{F}{A}$, which can be solved for using algebra. The wavefunction equations at $x = 0$ give the following expression for $\frac{B}{A}$:

$$\frac{B}{A} = \frac{1}{\sqrt{|p_2(0)|}}\left[\frac{C}{A} + \frac{D}{A} - \sqrt{|p_2(0)|}\right]. \tag{39}$$

Using this result, the derivatives of the wavefunctions at $x = 0$ give

$$\frac{C}{A} = \frac{D}{A}\left[\frac{|p_2(0)| - ip_1}{|p_2(0)| + ip_1}\right] + \frac{2ip_1\sqrt{|p_2(0)|}}{|p_2(0)| + ip_1}. \tag{40}$$

Using these two results, the wavefunction equations at $x = a$ give

$$\frac{D}{A} = \frac{\frac{F}{A}\sqrt{|p_2(a)|}(|p_2(0)| + ip_1)e^{i\frac{p_3}{\hbar}a+\phi(a)} - 2e^{2\phi(a)}ip_1\sqrt{|p_2(0)|}}{|p_2(0)| + ip_1 + e^{2\phi(a)}(|p_2(0)| - ip_1)}. \tag{41}$$

Evaluating the wavefunctions' derivatives at $x = a$, using the previous results, gives

$$\frac{F}{A} = \frac{2ip_1\sqrt{|p_2(0)||p_2(a)|}e^{-i\frac{p_3}{\hbar}a+\phi(a)}}{\sqrt{|p_2(0)|}+ip_1} \times \frac{2|p(0)|+2ip_1}{i\left(1+e^{2\phi(a)}\right)[p_3|p_2(0)|+p_1|p_2(a)|]+\left(1-e^{2\phi(a)}\right)[|p_2(0)||p_2(a)|-p_1p_3]} \tag{42}$$

.

The last variable, $\frac{F}{A}$, is the most important because it is directly related to the probability of an electron tunneling through the potential energy barrier. This probability is equal to the probability of being to the right of the barrier divided by the probability of being to the left of the barrier. As discussed in section 2.1.2, the probability of finding an electron at displacement x is given by $|\Psi(x)|^2$, meaning the probability of tunneling must be

$$T(x, E) = \frac{|F|^2}{|A|^2} \tag{43}$$

In order to solve for a more intuitive expression for $T(x, E)$, it is common to simplify the given scenario by making the approximation that $\Phi_A = \Phi_B \equiv U_o$ before the bias potential is applied, meaning that the potential energy barrier is represented by a square, as shown in Figure 14, and no longer has a linear function for potential energy in the region of the barrier. It is also common to leave the potential energies on either side of the barrier equal to zero.

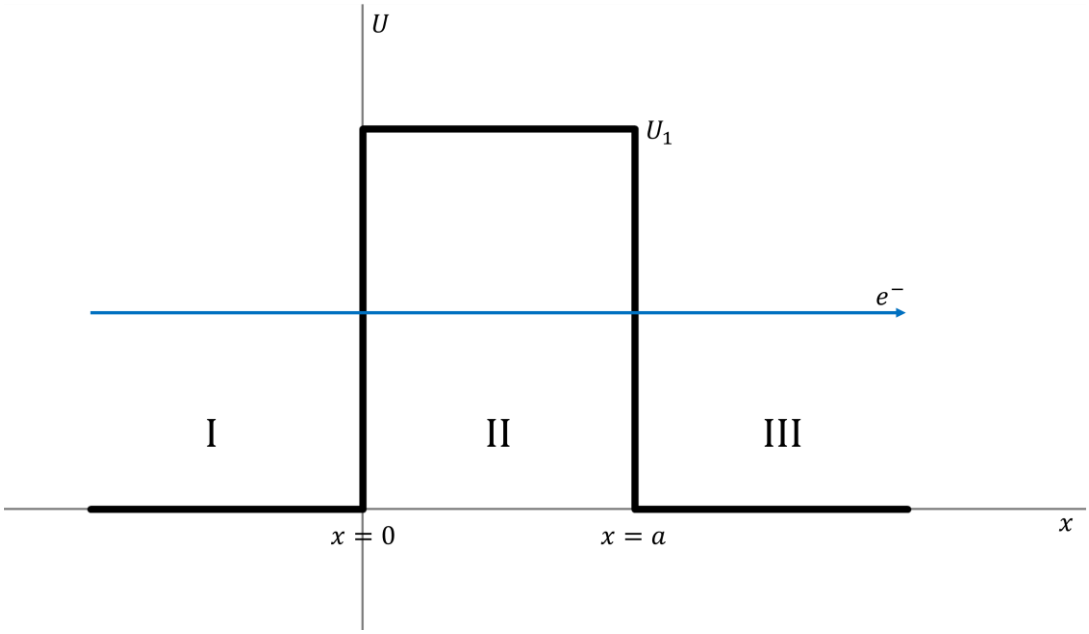

Figure 14. Potential energy barrier after approximations. Approximating the barrier as a square with a height of U_o, given by $\Phi_A = \Phi_B \equiv U_o$, and with zero potential energy on either side simplifies the expression for the tunneling probability to one that it more intuitive.

The results of these approximations are that $p_1 = p_3$ and $|p_2(0)| = |p_2(a)| \equiv p_2$. In addition to these results, the expression for $\phi(a)$ changes; $\phi(a)$ was represented by an integral, because the sloped barrier was approximated using a number of square barriers. However, now that the barrier is a single square, the integral is no longer needed, simplifying the expression for $\phi(a)$ to

$$\phi(a) = \frac{a}{\hbar}\sqrt{2m(U_o - E)}\,. \tag{44}$$

By applying each of these approximations, the derivatives of the wavefunctions at $x = a$ gives

$$\frac{F}{A} \approx \frac{4ip_1p_2e^{\phi(a)-i\frac{p_1}{\hbar}a}}{(1-e^{2\phi(a)})({p_2}^2-{p_1}^2)+i2p_1p_2(1+e^{2\phi(a)})}\,. \tag{45}$$

Lastly, for a wide barrier, $e^{2\phi(a)} \gg 1$. Using this approximation, the final expression for $\frac{F}{A}$ is

$$\frac{F}{A} \approx \frac{4e^{-\phi(a)-i\frac{p_1}{\hbar}a}}{2-i\left(\frac{p_1}{p_2}-\frac{p_2}{p_1}\right)}. \tag{46}$$

Now that an expression for $\frac{F}{A}$ is known, the definition of tunneling probability gives

$$T(E) \approx \frac{16e^{-2\phi(a)}}{2+\left(\frac{p_1}{p_2}\right)^2+\left(\frac{p_2}{p_1}\right)^2}. \tag{47}$$

Referring to equations (8), (15) and (44) for the definitions of p_1, p_2, and $\phi(a)$, respectively, simplifies this expression to

$$T(E) \approx 16\left(\frac{E}{U_o}\right)\left(1-\frac{E}{U_o}\right)e^{-\frac{2}{\hbar}\sqrt{2m(U_o-E)}a}. \tag{48}$$

Now that the probability of tunneling is known, a relationship between this and the tunneling current can be found. In simple terms, current is the number of electrons passing through a given area, so it would make sense if it was proportional to the probability of passing through a given area. We know the probability of tunneling is given by *T(E)* and that the probability a particle reaching the barrier would be given by $|\Psi(0)|^2$, so we can say that for a given energy E

$$I(E) \propto |\Psi(0)|^2 T(E)\,. \tag{49}$$

This relationship can be generalized even more by introducing Fermi energy levels. Essentially, the Fermi level is the highest probable energy state that an electron can exist at within a substance; in other words, it is improbable for an electron to exist above the Fermi level. For the sample side of the barrier the Fermi level is at 0 V, and for the probe side of the barrier the Fermi level is at U_1, because it is experiencing a bias voltage which shifts its Fermi level. Only electrons with energies between these two Fermi energies are free to tunnel through the barrier from region I to region III. If we want to know the total tunneling current, it would be the sum of the currents for each possible tunneling energy, given by

$$I \propto \sum_{U_1}^{0} |\Psi(0)|^2 T(E)\,. \tag{50}$$

To simplify this relation, the local density of states (LDOS) is introduced. General density of states describes the number of states with energy E_o in a given volume; this is used with homogenous substances and therefore does not depend on location. Since our thin films will not necessarily be homogenous, the LDOS is used, which gives the density of states for a given energy and location. The LDOS of the sample is given by

$$\rho(x, E_o) \equiv \frac{1}{eV} \sum_{E_o - eV}^{E_o} |\Psi(x)|^2 \,. \tag{51}$$

Using this definition of the LDOS, the tunneling current can be rewritten using the LDOS of the sample:

$$I \propto 16\rho(0,0)\left(\frac{E}{U_o}\right)\left(1 - \frac{E}{U_o}\right)(-U_1)e^{-\frac{2}{\hbar}\sqrt{2m(U_o - E)}a}. \tag{52}$$

From this equation it can be seen that tunneling current is directly proportional to the bias voltage applied to the sample and that it also decreases exponentially as the width of the barrier increases. Lastly and most importantly, the tunneling current can be used to learn about the LDOS of the sample. When scanning with an STM, a value for tunneling current will be measured at each point scanned, meaning that a value for the LDOS at each point can be obtained. By knowing the LDOS as each point, a general understanding of the composition of the film can be obtained.

2.3. Scanning Methods

When imaging a sample with an STM, there are two important variables to consider: current and distance from the sample. These two variables are what are manipulated during the imaging process to allows the probe to scan over the entire sample surface. In the general scanning method of the STM, shown in Figure 15, the probe is brought close to the sample, which is at a bias voltage relative to the probe, and it then scanned over the sample surface as electrons tunnel from the probe to the sample. There are, however, two specific scanning modes that can be used with the STM: constant–height and constant–current.

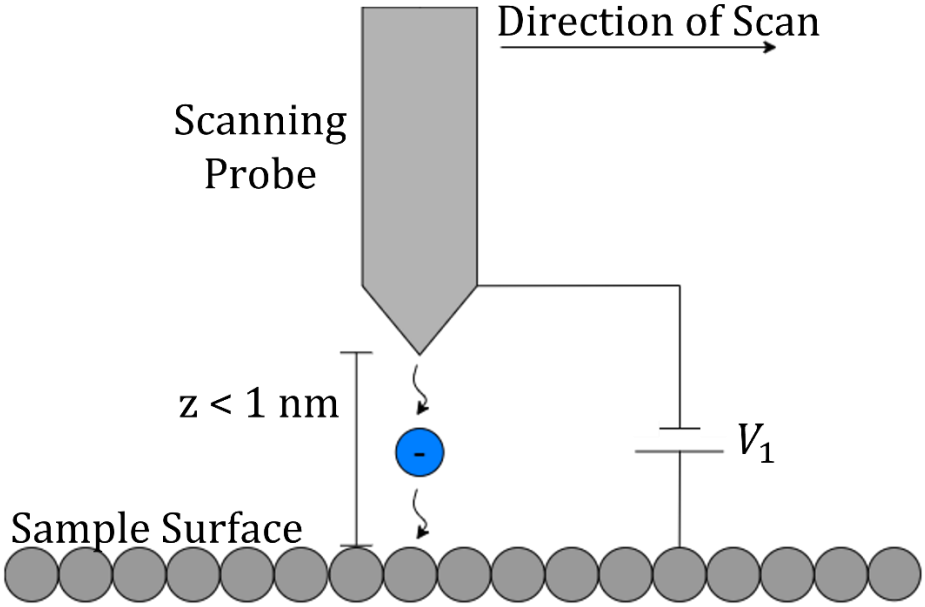

Figure 15. The general operation of the STM. The scanning probe is brought within angstroms of the sample surface, which is at bias voltage V_1. The probe is then moved along the surface in the direction shown while electrons tunneling from the probe to the sample.

As the name implies, in constant–height mode the distance between the scanning probe and the sample stage is held constant. When the probe is scanned over the sample in this manner, any change in surface topography will cause a change in the tunneling current. As a result, tunneling current becomes the important variable to measure and record, as it is the dependent variable in this scenario and the one used to generate the final image.

The other scanning method, and the one that will be used in the Houghton University STM, is the constant–current mode. In this mode, the current is held constant at a set value and the height is free to move throughout the scan. As the probe scans over the surface, if there is a change in topography the probe will move up or down in order to keep the current at the set value. Therefore, in this method, the height is measured and recorded, and used to generate the final image.

The reason constant–current mode will be utilized is because it is safer and more precise than constant-height mode. In constant–current mode, a current feedback loop is required because the STM needs to be able to read the current at every point to make sure that it

accurately adjusts the probe height to maintain the set current. This feedback loop slows down the scanning process, but as a result it allows the scan to be more precise, especially over samples that do not have a flat surface. In addition to precision, since the probe is allowed to move up and down in constant–current mode, there is a much lower chance that the probe will come in contact with the surface, avoiding any damage to both the sample and the probe.

2.4. Vibration Damping

Since the STM is dealing with extremely small and precise measurements, it will need to be isolated from outside vibrations to avoid noise in the measured data. The building the STM is located in will have some resonant frequency of its own, so the STM will need to have a way to mitigate this frequency in a manner that causes it to have a low resonant frequency. The goal of this frequency is ~1 Hz because that would help prevent sudden movements of the STM. Two types of vibration damping are utilized: springs and eddy currents.

Spring damping works by means of Hooke's Law, which states that

$$F_r = -KX \tag{53}$$

where F_r is the spring restoring force, X is the spring's displacement from equilibrium, and K is the spring constant given by

$$\nu = \frac{1}{2\pi}\sqrt{\frac{K}{M}} \tag{54}$$

where M is the mass. Since the goal is a 1 Hz resonant frequency for the STM, this equation becomes

$$K = (2\pi)^2 M \tag{55}$$

By knowing the mass that each spring will be holding, the spring constant needed to achieve 1 Hz can be calculated.

Eddy current damping works by means of Faraday's Law

$$\varepsilon = -\frac{d\phi}{dt} \tag{56}$$

stating that a change in magnetic flux, ϕ, will result in an induced voltage, ε, and therefore an induced current, I, as shown in Figure 16. Diagram showing

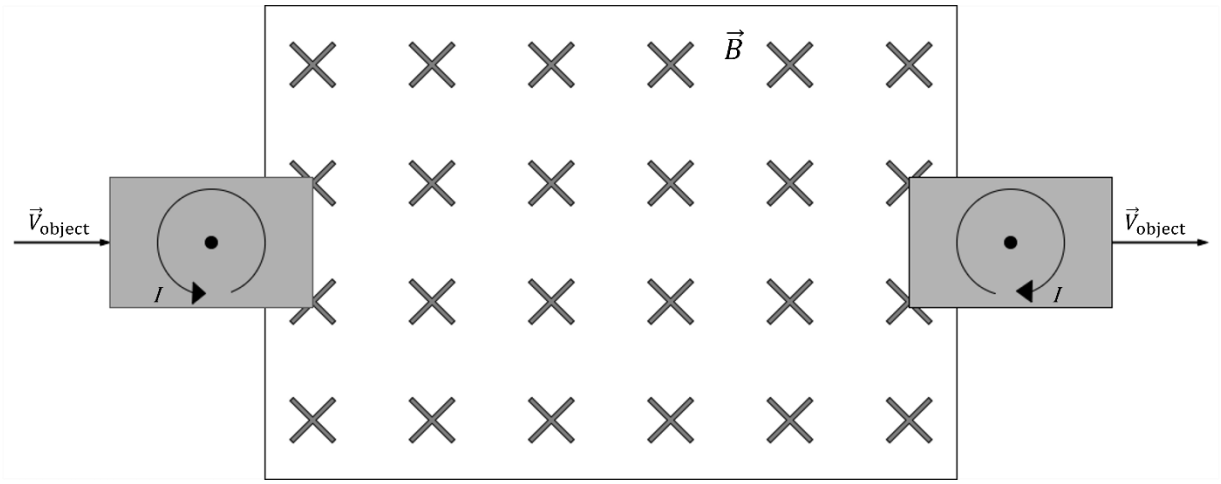

Figure 16. Diagram showing theory of Eddy current damping. As a conductor moves into a magnetic field $\vec{Y}$ with velocity $\vec{V}_{object}$, a current I is induced in the conductor, causing its electrons to have velocity $\vec{V}_e$. This velocity results in a Lorentz force that opposes $\vec{V}_{object}$, slowing down the object.

As a result of this current, the electrons in the conductor have a velocity as shown by $\vec{V}_e$. This velocity within the magnetic field causes a Lorentz force to oppose the motion of the conductor. This Lorentz force is given by

$$\vec{F} = -e\left(\vec{V} \times \vec{Y}\right) \tag{57}$$

where $\vec{F}$ is the Lorentz force, e is the charge of an electron, $\vec{V}$ is the velocity of the particle and $\vec{Y}$ is the magnetic field. It can be seen from this equation and from the figure, that the force will be directed to the right when the conductor is moving to the left, reducing its velocity. Therefore, by having magnets attached to the STM, a magnetic field will be generated that will cause a Lorentz force to resist any motion of the STM, thereby damping vibrations it may experience.

Chapter 3

AMBIENT–AIR SCANNING TUNNELING MICROSCOPE

3.1. Apparatus

The STM has three main components to its physical structure: the vibration–damping system, the sample stage, and the scan head. The vibration–damping system uses spring and magnets to reduce the vibrational noise from the STM's surroundings. The sample stage houses the thin metal film and the stepper motors; the scan head is held by the sample stage and contains the scanning probe and the preamplifier.

3.1.1. Vibration–Damping System

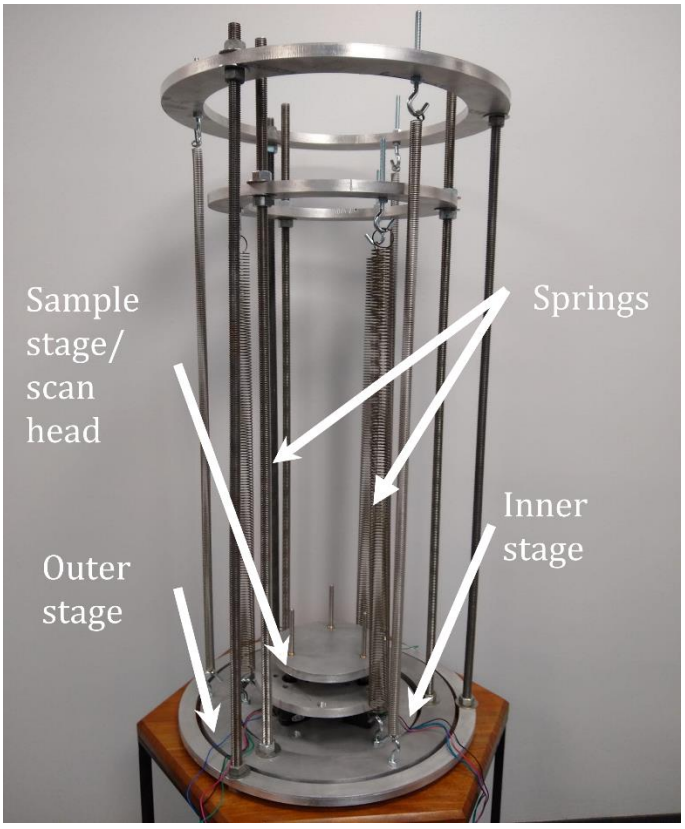

Figure 17. Photograph labeling the components of the vibration–damping system. It is a three–stage system, with the sample stage resting on the inner stage, which is suspended from the outer stage by springs, which is suspended from the base by more springs. The upper section of each stage is held in place by threaded rods extending from the lower section of the stage.

The vibration––damping system consists of one full round 1.27–cm–thick Al plate (component1) and four 1.27–cm–thick Al rings (components 2-5); the dimensions of each piece are given in Table 1. Each piece is held up by the other pieces using a combination of springs and threaded rods, as shown in Figure 17. Component 1 is suspended by springs from component 2, which is held up by threaded rods on component 3. Component 3 is then suspended by more springs from component 4, which is in turn held up by threaded rods from component 5, which rests on a table. The springs are connected to each piece using 0.25 in.–20 × 4.25 in. clothesline hooks that have been cut shorter, since each component is only 1.27 cm thick. The springs holding component 1 have a spring constant of 29.77 N/m and the springs holding component 3 have a spring constant of 52.54 N/m. With these spring constants and using the calculations discussed in section 2.4, the inner stage will have a resonant frequency of ~0.697 Hz and the outer stage will have a resonant frequency of ~0.674 Hz.

Table 1. Dimensions of each of the aluminum pieces used in the vibration-damping system.

Component #	Outer Diameter	Inner Diameter
1	25.4 cm	N/A
2	30.48 cm	20.32 cm
3	35.56 cm	25.4 cm
4	40.64 cm	30.48 cm
5	40.64 cm	35.56 cm

3.1.2. Sample Stage

The sample stage is made of 1.27–cm–thick aluminum and has a diameter of 20.32 cm. There are three 2.54 cm holes in the sample stage to allow the three 0.25 in.–80 × 4 in. threaded rods and couplers attached to the motors to pass through. Each motor is mounted to the sample stage with four 4-M3 screws and the hole for each screw is recessed by 0.635 cm so that the surface can remain flush. In addition to each of these holes, there are three more holes in the sample stage that have been threaded so that it can be mounted to

piece 1 with threaded rods. In the center of the sample stage, the thin metal film sample will be mounted, but the mounts have not yet been designed.

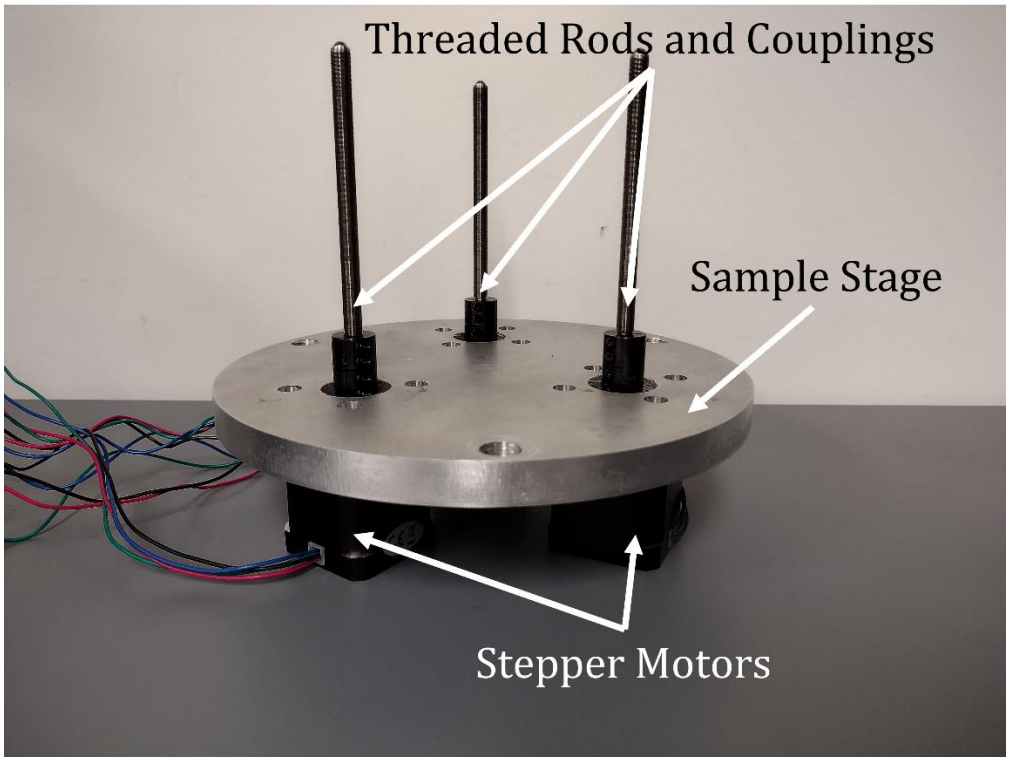

Figure 18. Photograph labeling the parts mounted on the sample stage. The stepper motors are mounted to the bottom of the sample stage through holes in the sample stage. The threaded rods are mounted to the stepper motor shafts using couplings. The wires from the stepper motors are connected directly to the stepper motor drivers.

3.1.3. Scan Head

The scan head is made of 1.27–cm–thick aluminum and has a diameter of 15.24 cm. There are three 0.953 cm holes in the scan head where threaded bushing have been placed and secured by Loctite 680 Retaining Compound. The threading of these bushings match that of the threaded rods on the stepper motors, and the scan head is attached to the sample stage via these bushings and rods. When the stepper motors are rotated, the scan head moves up and down the rods as they thread in and out of the bushings.

Because the low tunneling current (~1 nA) is susceptible to noise, the preamplifier is mounted on the scan head using #4-40 screws. It is electrically insulated from the scan

head by plastic spacers that the screws pass through. Also mounted with #4–40 screws and plastic spacers is the 201–0017–01 Universal DIP Adapter board. This board is essentially a through–hole breadboard; female pin connectors are soldered to the DIP board holes, and it acts as a gathering point for all the wires that need to leave the scan head.

The piezo buzzer is mounted to the center of the scan head using two washers. Each washer has a groove cut through the center of the flat side, to allow pass–through for the wires connecting to the piezo electrode quadrants. Each washer has three semicircular grooves cut out of their edges, so that three #4–40 screws can be used to mount them to the scan head; this allows for easy removal and mounting of the piezo buzzer.

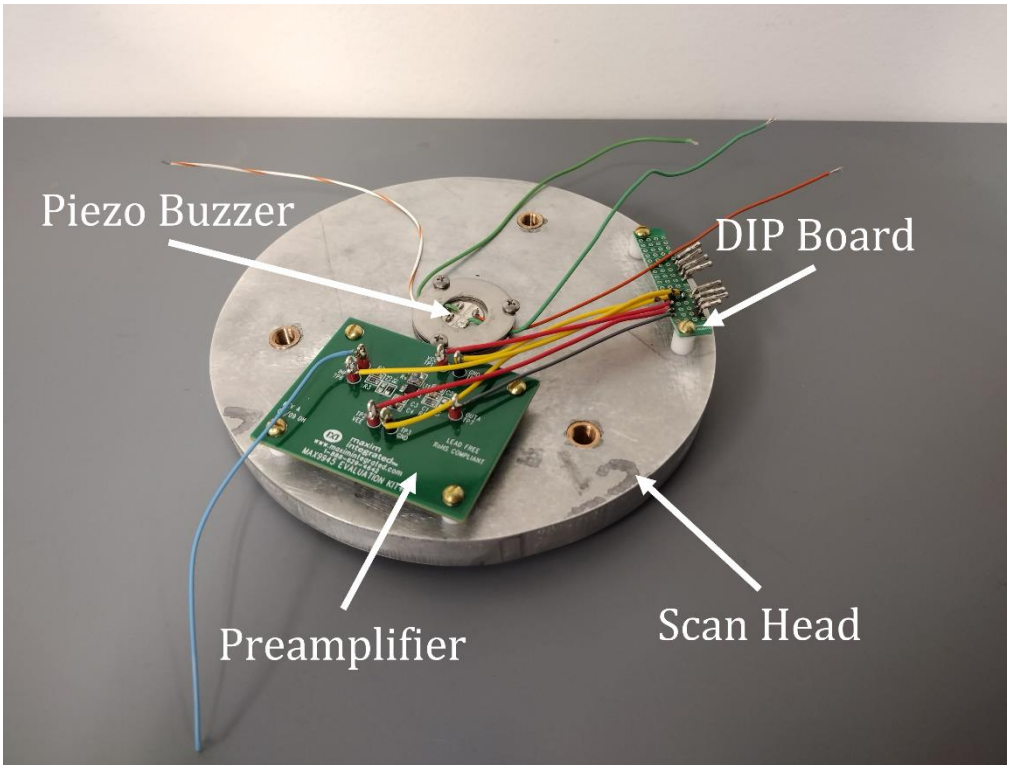

Figure 19. Photograph labeling the parts mounted to the underside of the scan head. The preamplifier is mounted close to the scanning probe to reduce noise in the tunneling current; it is insulated from the scan head by plastic spacers. The piezo buzzer is mounted to the scan head by placing it between two washers which are mounted to the scan head. The DIP board gathers all of the wires on the scan head so that can be routed to the rest of the circuit.

The piezo buzzer controls the three–dimensional motion of the scanning probe. In a piezo buzzer, a piezoelectric ceramic layer is mounted on an electrode, with another electrode mounted on the top. When a positive voltage is applied to the ceramic, it expands outward, increasing its radius; however, since the ceramic is rigidly mounted to the bottom electrode, they must both bend into a bowl shape, with the piezo on the outside, to adjust for this change in radius. When a negative voltage is applied, the opposite happens; the ceramic and bottom electrode must bend into a bowl once again, but with the ceramic on the inside, since it decreases its radius by contracting. Since the top electrode is much thinner than the other two layers, it does not produce much strain on the ceramic, allowing it to still bend. In order to achieve movement in three dimensions, the electrode on the buzzer is cut into four quadrants, so that each quadrant controls a different section of the buzzer, as shown in Figure 20. When a voltage is applied to one of the quadrants, only the region of the piezoelectric material underneath that quadrant will expand/contract. Adding voltages in different combinations to the quadrants gives the probe full range of motion in each direction.

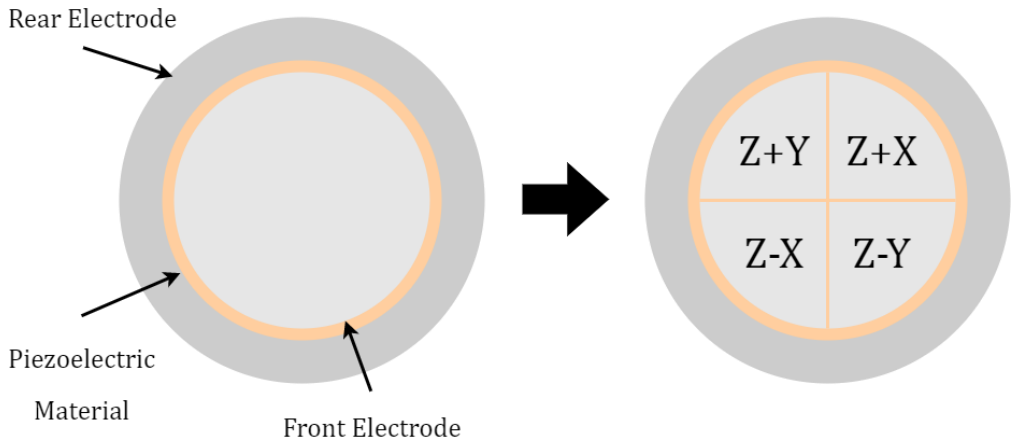

Figure 20. Diagram showing how to achieve (x,y,z) motion with a piezo buzzer. By cutting the front electrode into four quadrants, each quadrant controls a different direction in the xy-plane, while all together they control the z-direction. With the probe attached in the center, the probe can move in all directions.

The STM achieves scanning probe motion in the x–direction by applying a voltage to both the Z+X and Z-X quadrants; for the case when Z is held at zero and X is kept positive, the

Z+X quadrant will have a higher applied voltage and, therefore, will expand, while the Z-X quadrant will contract. This causes a slope on the center of the piezo, as shown in Figure 21, causing the scanning probe to tip to one side; the same process is performed for motion in the y–direction. In order to move the scanning probe in the z–direction, the STM uniformly applies a voltage to each quadrant, which causes each one to expand by the same amount. In an example [29] of a piezo buzzer being used in this way, the buzzer had a total vertical range of motion of ~40 μm and a total lateral range of motion of ~60 μm. This buzzer is used instead of the piezo drive discussed in Section 1.3 because it can be used at lower voltages than the piezo drive; this buzzer has a maximum peak-to-peak voltage ($V_{p\text{-}p}$) of 15 V while the piezo drive used a waveform of 1000 V pulses. In addition to utilizing low voltages, the piezo buzzer is also inexpensive, costing only $0.96 per unit, making it affordable to replace or replicate.

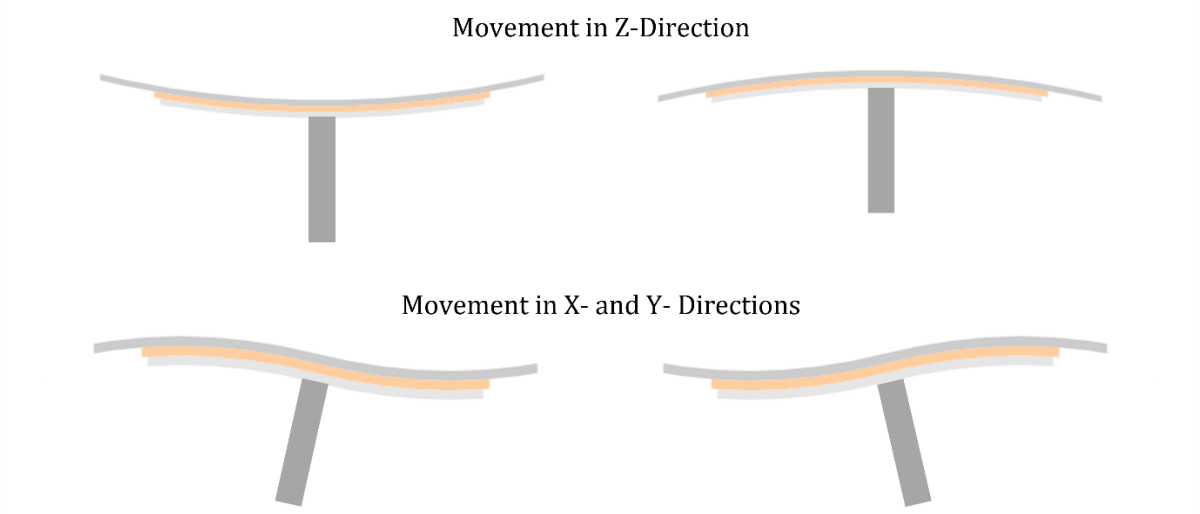

Figure 21. Diagram showing piezo buzzer moving in three dimensions. Motion in the z–direction is achieved by uniformly applying voltage to all four quadrants at the same time, resulting in them all expanding or contracting by the same amount. Motion in the x–y plane is achieved by applying voltages to opposing quadrants, which in the case above for Z equal to zero, results in one side expanding and the other side contracting, causing a slope in the center of the piezo, tipping the scanning probe to one side.

3.1.4. Scanning Probe

The scanning probe is made from a ~1–cm–long thin stainless steel rod with a ~5–mm–deep hole, 0.17 cm in diameter, in one end. A female pin connector is glued into this hole, so that an STM tip can be placed in the pin. A small ceramic disk is connected to the base of the rod to act as an insulator between it and the piezo electrodes. The steel rod with the other components is then secured to the center of the piezo buzzer, so that it is contacting all four quadrants of the electrode. A wire is connected to the tip of the scanning probe, which leads directly to the input of the preamplifier.

3.2. Electronics

The circuit for the STM consists of three sections: sending voltages, receiving data, and controlling motors. Each section is controlled by a Teensy 4.1 microcontroller, as shown in Figure 22, which is operated using the Arduino software; it also operates on a 3.3 V basis, meaning its pins can input and output between 0–3.3 V. The Teensy is used instead of an Arduino because of its faster clock speed of 600 MHz compared to an Arduino's 16 MHz clock speed. The Teensy communicates with other parts of the circuit using serial peripheral interface, or SPI. Using SPI allows the Teensy to easily communicate with numerous other electronics and also gives it the ability to choose which electronics it communicates with. This SPI communication can transfer data at up to 60 Mbps and operates using four pins: master–in–slave–out (MISO), master–out–slave–in (MOSI), chip select (CS) and clock (SCK), with the Teensy being the master and the other electronics being the slaves, with each slave electronic needing its own separate CS pin from the master. The MISO pin is for data transfer from slave to master, the MOSI pin is for data transfer from master to slave, SCK runs the clock of the slave and CS allows the master to choose which slave to communicate with, making it easy to handle data from numerous sources.

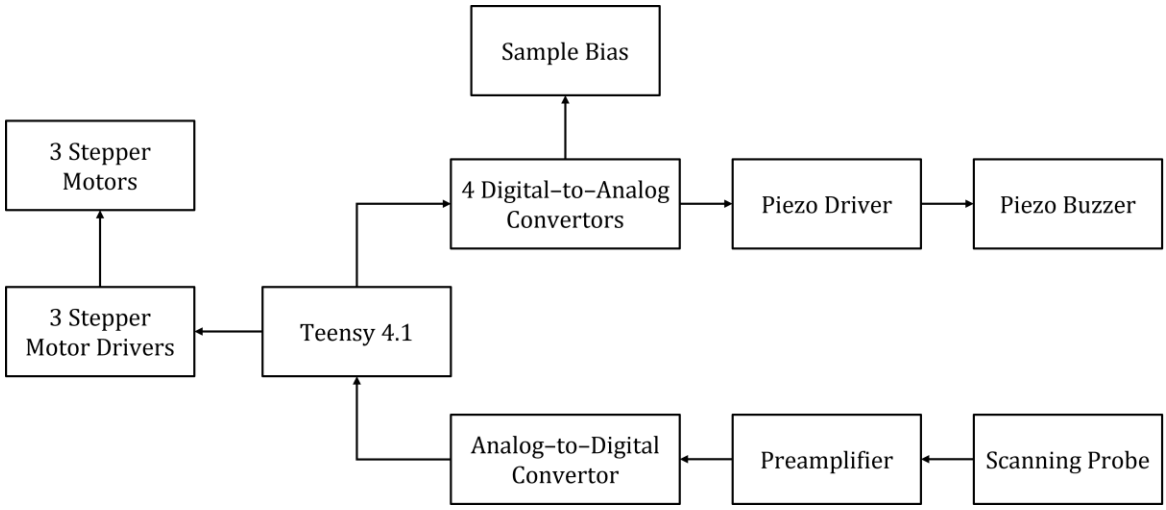

Figure 22. Block diagram showing simplified circuit for the STM. It shows each portion of the circuit separately: sending voltages (top right), receiving data (bottom right), and controlling motors (left). The Teensy microcontroller is the center of the circuit, as it is what handles all of the data and controls the rest of the circuit.

3.2.1. Receiving Data

The first step in the circuit for receiving data, shown in the bottom right of Figure 22, is the scanning probe sending the tunneling current to the MAX9945AUA+ operational amplifier (op–amp) mounted on the MAX9945 Evaluation Kit+ board, which acts as the preamplifier for our circuit, as shown in Figure 23. The feedback resistor for this op-amp originally has a value of 100 kΩ, and this determines the level of amplification the op-amp can provide. However, since the input current will be so small, on the nano–amp scale, the 100 kΩ feedback resistor was replaced with a 100 MΩ resistor. An OPA2228P op–amp with two equal–value resistors is placed on the output to invert the output back to a positive value, without amplifying it.

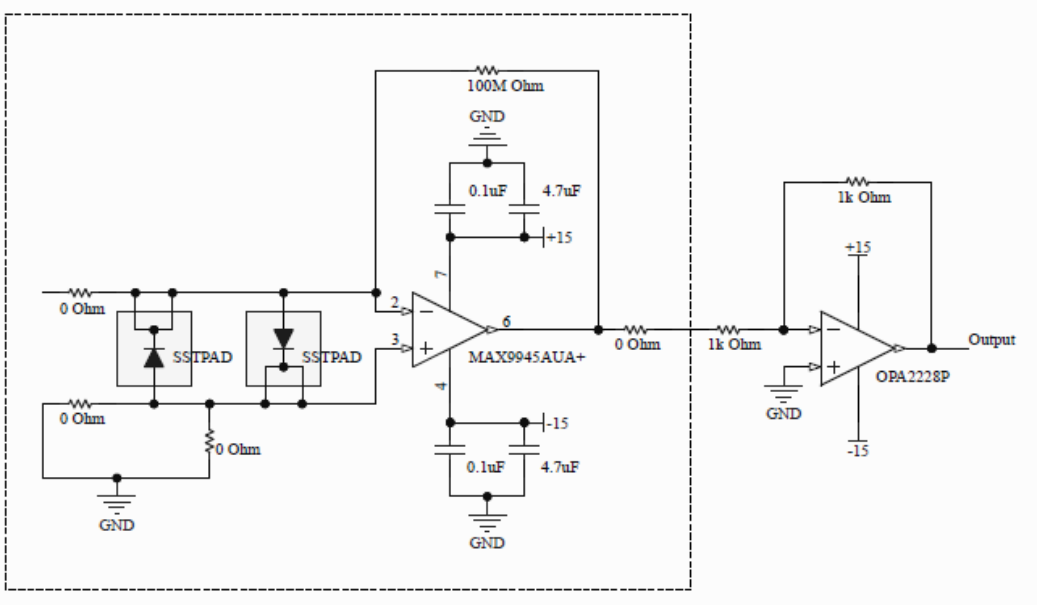

Figure 23. Circuit for the MAX9945AUA+ op–amp with new feedback resistor. The original feedback resistor had a value of 100 kΩ, but it was increased to 100 MΩ to ensure the nano–amp input was amplified to an output in the amp scale. The section inside the dashed line is the circuit that is constructed on the MAX9945 Evaluation Kit+ board. The input is directly connected to the scanning probe. The output is put through an OPA2228P op–amp with equal resistors to invert the output back to positive without amplifying it.

The output of the preamplifier is sent to the TLC4541ID 16 bit analog–to–digital converter (ADC) to be converted back into a digital voltage for the Teensy to read, shown in Figure 24. This ADC has a maximum clock speed of 15 MHz and communicates with the Teensy through SPI. It has an operating voltage, V_{DD}, range of 4.5 V to 5.5 V and a reference voltage, V_{REF}, range of 4 V to V_{DD}, each of which are set to 5 V, and the range for the analog input is 0 V to 5 V. Both the analog input and the digital output lines need to have an impedance to ground of a 1 MΩ resistor in parallel with a 20 pF capacitor; this is the impedance of the oscilloscope used in testing, because it was found that the circuit worked correctly when measured with the oscilloscope. The output of the ADC is not sent directly to the Teensy, however, since the ADC operates on a 5 V basis and the Teensy uses a 3.3 V basis. To resolve this issue, the output is passed through a TXS0108E 8-bit voltage translator, which works by setting one group of pins to 5 V and the other set of pins to 3.3 V, which converts voltages from a 5 V basis to a 3.3 V basis. This allows the Teensy to be able to input the digital voltages from the ADC.

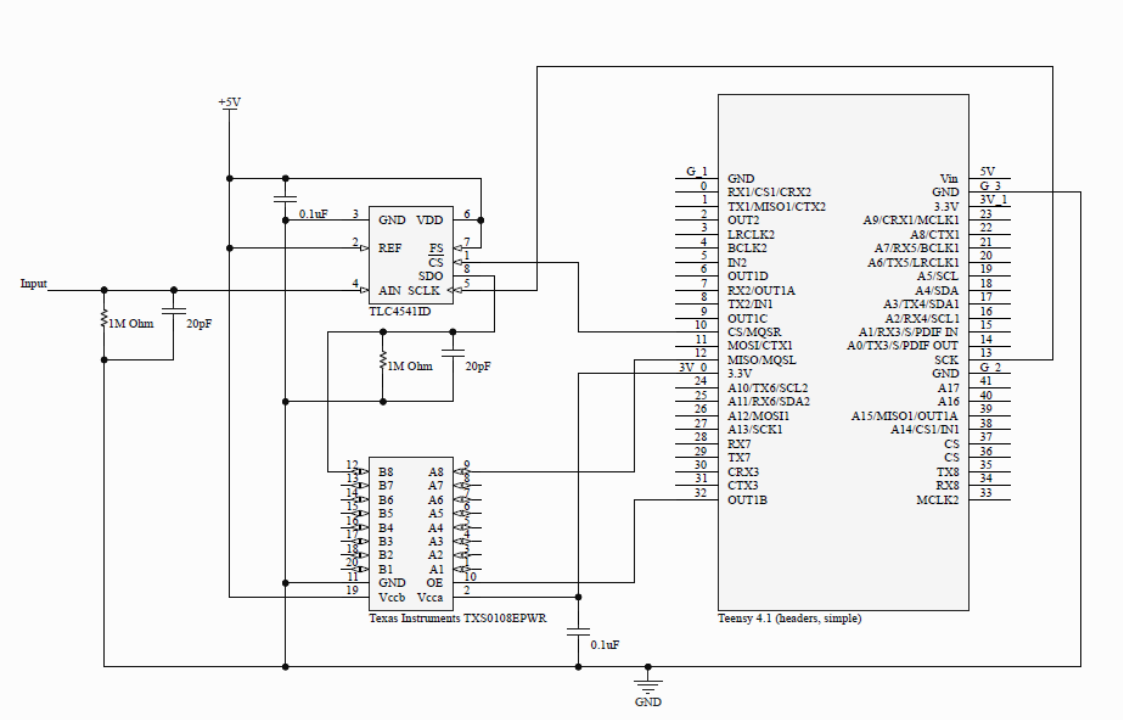

Figure 24. Circuit showing TLC4541ID ADC connection to Teensy 4.1. The ADC uses a 5 V reference voltage so that the same source can be used for V_{REF} and V_{DD}. The output of the ADC must be sent through the TXS0108E voltage translator since the ADC uses a 5 V basis and the Teensy uses a 3.3 V basis.

3.2.2. Sending Data

The block diagram for sending voltages to the STM is shown in the top right section of Figure 22 and includes four MAX5719AGSD+ 20–bit, digital–to–analog converters (DAC), a homemade piezo driver circuit and an AB1560B piezo buzzer. The first step is for the Teensy to send digital voltages to the DACs over SPI, shown in Figure 25, so that they can be converted to analog voltages that other electronics can use. SPI sends data in 8–bit groups, so for the DAC to operate using 20–bits, the Teensy must send 24 bits to the DAC (three separate SPI communications), and the DAC takes the first 20 bits to convert to an analog value. The DACs have a maximum clock speed of 50 MHz and operate on a 5 V basis with a 4.5–5.5 V_{DD} input range, with a 4.0–V_{DD} reference voltage, V_{REF}, input range. The input high voltage for the DAC pins is given by 0.7 V_{DD}, meaning that in order for the Teensy's 3.3 V to be able to trigger high on the DAC, V_{DD} must be set to less than or equal to ~4.7 V; the reference voltage is also set to 4.7 V so that the same source can be used for

each. The Teensy sends data for the movement of the piezo to three of the DACs, and it sends the sample bias voltage to the fourth DAC. For the DACs handling the piezo movement data, each DAC is sent a value corresponding to a dimension of movement of the piezo: X, Y, and Z.

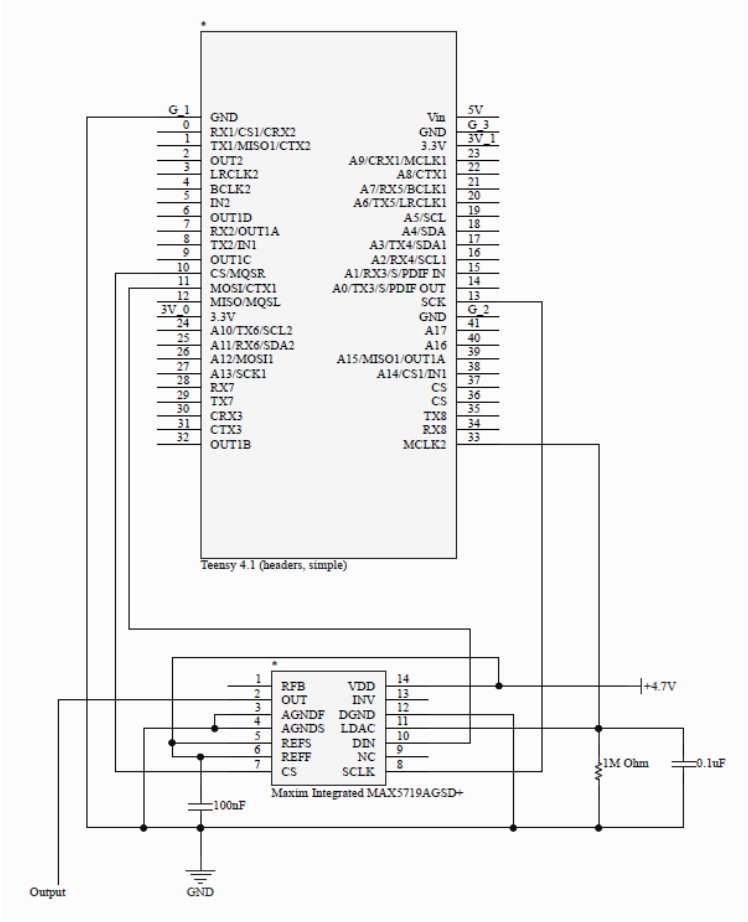

Figure 25. Circuit showing MAX5719AGSD+ DAC connection to Teensy 4.1. Digital voltages are sent from the Teensy to the DAC using serial peripheral interface, or SPI. The supply voltage for the DAC is set to 4.7 V so that the 3.3 V from the Teensy can trigger high on the DAC pins, and the reference voltage is set to the same value. Output will either be sent to a piezo driver circuit or the sample bias.

In the second portion of the circuit for sending voltages, the DACs send the voltages it received from the Teensy to the piezo driver circuit and to the sample, as shown in Figure 26. The DAC handling the sample bias is directly connected to the sample so that it can be held at a constant voltage for the entirety of the STM scan. The other three DACs are each connected to one of the inputs of the piezo driver. The piezo driver uses two OPA2228P

Integrated Circuits (ICs) to act as an adding and subtracting circuit. Each OPA2228P contains two op-amps, resulting in four total op–amps and four total outputs: Z+X, Z-X, Z+Y and Z-Y, as shown in Figure 26, with the values of X, Y, and Z being voltages. Two of these op–amps handle the outputs with X values and the other two handle outputs with Y values, meaning each OPA2228P handles a separate direction in the xy–plane, as can be seen from the pin labels in Figure 26. Each of these outputs is connected to a quadrant of the piezo buzzer. When a value for Z is applied, each quadrant will receive voltage, meaning the entire piezoelectric material moves together. When either an X or Y value is applied, opposite quadrants will move in equal, but opposite, amounts symmetric about the Z value.

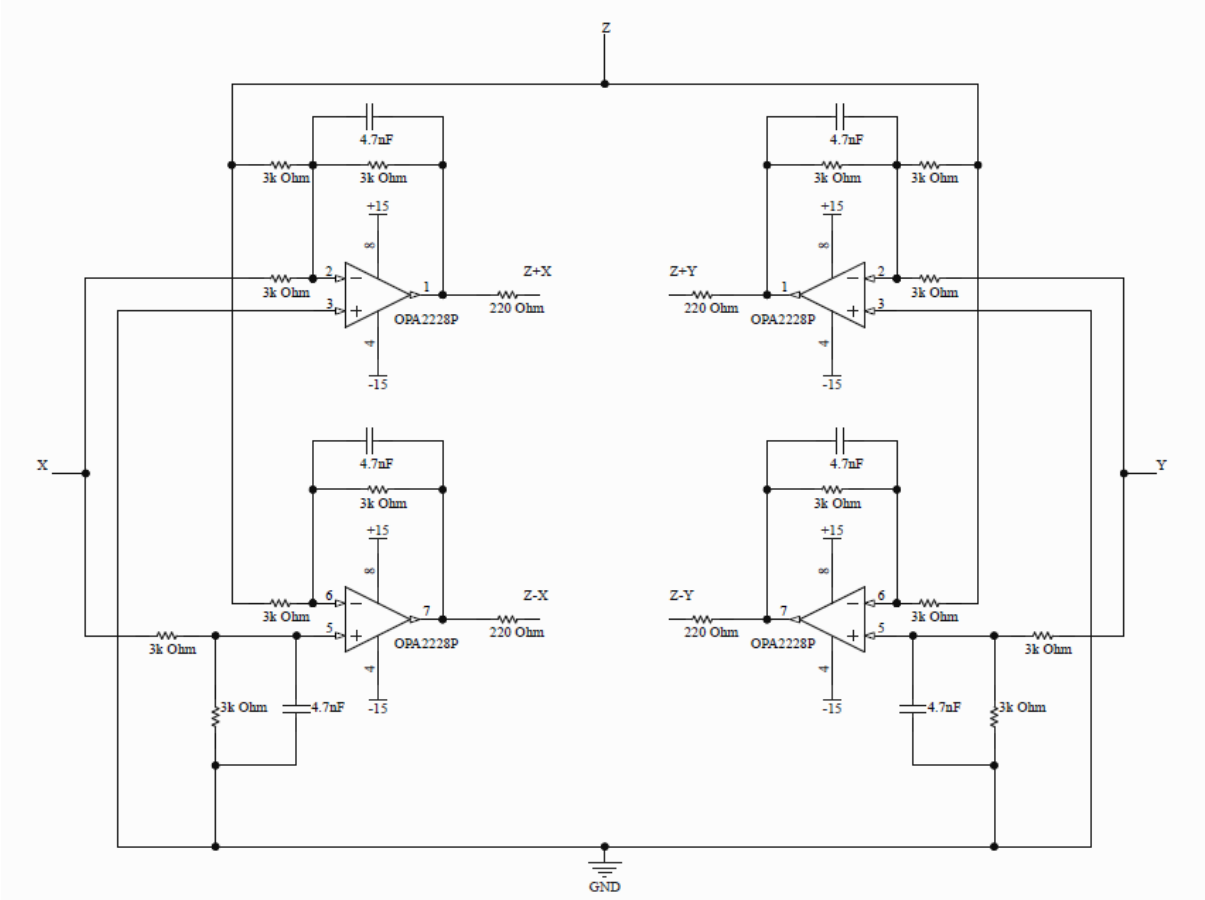

Figure 26. Circuit design for the homemade piezo driver. Each of the three inputs (X, Y, Z) comes from a separate DAC, and uses OPA2228P op–amps to operate as an adder/subtracter for these inputs. Each of the four outputs is then connected to the piezo buzzer to control its three-dimensional movement.

3.2.3. Stepper Motors

The STM uses three 17HM19-1684S 4–wire, bi–polar stepper motors to bring the scan head close to the sample so that the scanning probe is in range to perform a scan. The stepper motors use an input voltage of 12–24 V with a current of 1.68 A and a full step angle of 0.9°, giving it 400 steps per revolution (pul/rev). The stepper motors are each controlled by a TB6600 stepper motor driver, shown in Figure 27; this driver controls the direction and the turn speed of the motor. The stepper motor drivers have a supply voltage range of 9–42 V, so 15 V is used since that voltage is used elsewhere in the circuit. Each of the pins on the driver operate on a 5 V basis, so an SN74ACT241N 5 V buffer is used to allow the Teensy pins to trigger the driver pins. On the driver, the DIR- pin controls the direction of rotation and the PUL- pin controls the speed of the rotation; the ENA- pin is held at GND to prevent it from entering the free-rotation state. The driver also has six ON–OFF switches that control its settings: SW1, SW2, SW3, SW4, SW5 and SW6. SW1, SW2, and SW3 control the pulses per revolution (pul/rev) of the motor, and are set to ON, OFF, OFF, respectively, so that the pul/rev are set to 800, resulting in a microstep angle of 0.225° for these motors. SW4, SW5, and SW6 control the current supplied to the motor and are set to ON, ON, ON, respectively, so that the driver supplies 0.5 A. This is the minimum current that the drivers can supply, but since the motors can handle up to 1.68 A, this value can be increased if desired.

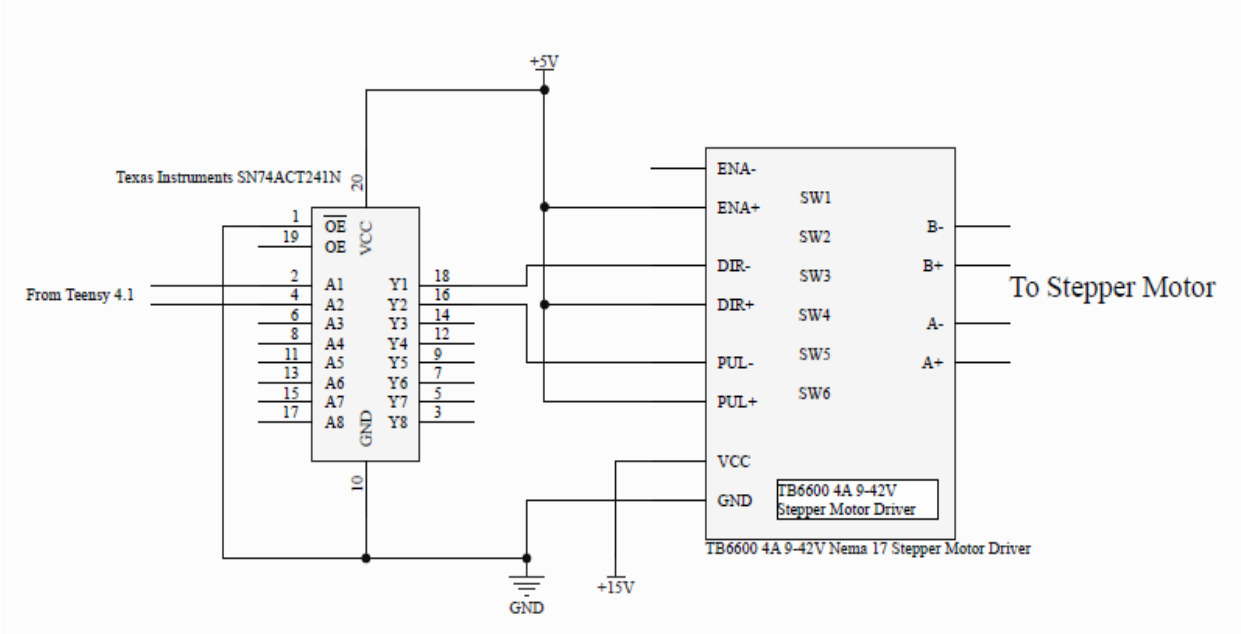

Figure 27. Circuit showing Teensy 4.1 connection to TB6600 stepper motor driver. The pulses from the Teensy must be sent through the SN74ACT241N 5 V buffer so that they can trigger the driver pins. Using the driver, the Teensy can control the direction and speed of the motor. The motor driver can also control the step size and the supply current for the stepper motor.

As stated in section 3.1.2, the threaded rods connected to the motors have 80 threads per inch (TPI), meaning that in 80 revolutions, the rods will move the scan head and scanning probe 2.54 cm. A 0.225° microstep from a single motor results in a ~66 nm vertical movement of the scanning probe. If all three motors take a single microstep together, the scanning probe will move ~198 nm.

3.3. Operation of the STM

The operation of the STM follows three steps: input parameters for the scan, start the scanning probe's approach to the sample, then scan the sample. The user interface for controlling the STM is done using Processing, an open–source programming software that runs on a computer's CPU as opposed to a microcontroller. A code written in Processing can produce an on-screen interface that is capable of inputting both keyboard and mouse commands. This interface is used for parametric input and to control the STM operation, including both manual and automatic control of the scanning head and scanning probe.

The first step in operating the STM is to input parameters regarding the calibration of the piezo movement, i.e., how far the piezo moves per volt applied, the bias voltage for the sample, and the target value for the tunneling current to maintain during the scan. After the parameters have been defined, the tip must be brought close to the sample until the target tunneling current is achieved. A two–step approach is used to bring the scanning probe close to the tip. First, in the rough approach, a camera visual feed displayed in Processing is used to manually guide the stepper motors to bring the scan head close to the sample. Then, in the automatic fine approach, the probe position is manipulated by the piezo buzzer until the target current is achieved. If the probe is extended to the limit of the piezo buzzer's range without reaching the target current, it is brought back to its starting position and one of the stepper motors moves one step forward, and the process is repeated until the target current is achieved. Since a single microstep of one motor moves the probe 3 orders of magnitude less than a full extension of the piezo, this fine approach can be done without risking the probe crashing into the sample.

Once the probe is close enough to the sample to maintain the target current, the scan is started. The Teensy's digital voltage output is split into 256 increments, resulting in 256 increments in both the x– and y–direction (0 to 255). The probe starts at (0,0), the top left corner, and scans across the full 256 points in the x-direction twice, once forward and once backward. It then moves up one y-increment and repeats the two scans in the x-direction. It continues in this manner until each point has been scanned twice, ending at the point (0, 255), the bottom left corner. The STM measures the current at each point it scans and corrects itself back to the target current by adjusting the probe height an amount calculated by the Teensy, using the current measured by the STM. Once the scan is complete, the current data is used to calculate the probe height at each point. Using this data, Processing generates two intensity plots, one for each direction, each representing an image of the sample surface. Since a 20-bit DAC is being used, the probe is not limited to a 256 by 256 area but can be moved anywhere within a 2^{20} by 2^{20} area. As a result, this allows the STM to produce multiple images of different parts of the sample without needing to move the sample. It also allows images larger than 256 by 256 to be taken, with each image size being a subset of the 2^{20} by 2^{20} area.

Chapter 4

TESTING AND RESULTS

4.1. Preamplifier Testing

In order to test the preamplifier's performance with nanoamp current inputs, a power supply was connected to a 10 GΩ resistor, which was then connected to the preamplifier input. As discussed in section 3.2.1, the feedback resistor for the preamplifier has been changed from a 100 kΩ resistor to a 100 MΩ resistor. With the combination of the 10 GΩ and 100 MΩ resistors, the preamplifier output was given by

$$V_{\text{out}} = -0.01V_{\text{in}} . \tag{58}$$

With an input range of 0–30 V, in steps of 1 V, the preamplifier output is shown in Figure 28. The important information provided by this graph is that the slope is a straight line, meaning the preamplifier has a constant conversion of current to voltage. The difference in slopes is likely due to a difference between the negative and positive inputs of the preamplifier op-amp; if the negative input was not actually at 0 V, then the current would be different, causing a difference in slope with the measured data.

Another test was performed with the preamplifier, along with the op-amp that follows it (shown in Figure 23) For this test, the 10 GΩ resistor was replaced with a 500 MΩ resistor, resulting in the output voltage being given by

$$V_{\text{out}} = 0.2V_{\text{in}} , \tag{59}$$

which is positive because the second op-amp is in place to invert the output of the preamplifier. With input voltages ranging from 5–30 V, in steps of 5 V, the output voltage is shown in Figure 29. The output values for this test are also shifted; they are shifted by 250 mV at an input of 5 V and by -160 mV at an input of 30 V.

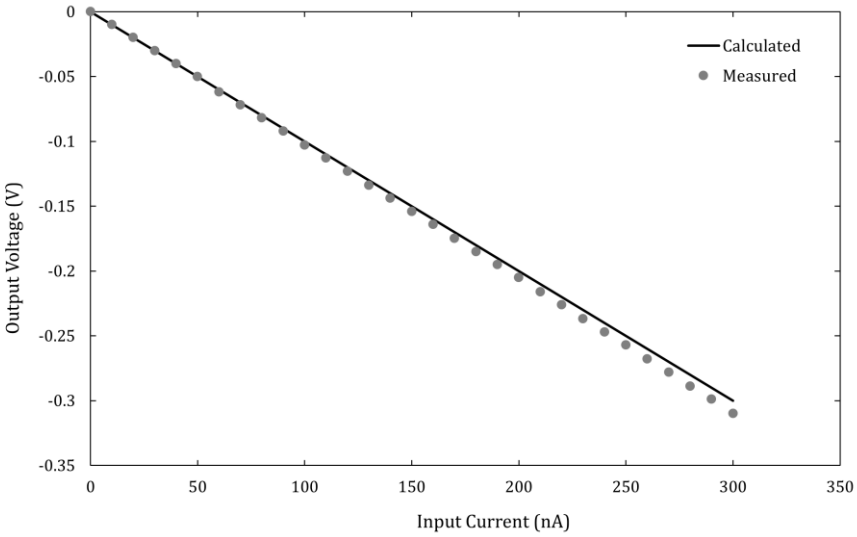

Figure 28. Graph showing preamplifier output voltage as a function of input current. Voltages were put through a 10 GΩ resistor to produce an input current on the order of nano-amps, to simulate a tunneling current. The slope of the measured line is constant, verifying that the preamplifier conversion of current to voltage is also constant. The measured slope is shifted most likely due to a difference between the negative and positive inputs of the preamplifier op-amp.

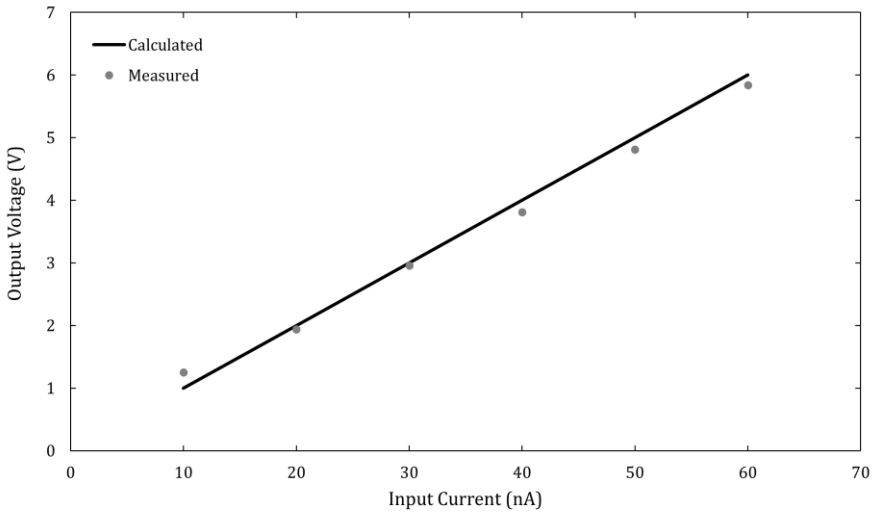

Figure 29. Graph showing preamplifier and op–amp output voltage vs input voltage. Input voltages were put through a 500 MΩ resistor to produce a current on the scale of nano-amps. The measured output is shifted from the calculated output most likely due to a difference between the negative and positive inputs of the preamplifier op-amp.

4.2. Piezo Driver Testing

The piezo driver was tested by connecting each of the three inputs to a separate power supply and measuring the voltage on each of the four outputs with different combinations of inputs; the results of this test are given in Table 2. The output values are negative because each op-amp in the circuit is set up to be an inverting amplifier, but the numerical value of each output is correctly given as the sum or difference of the inputs.

Table 2. The results for the piezo driver circuit test. The left three columns are the input voltages for the circuit and the four right columns are the output voltages of the circuit, which are the sums and differences of the inputs.

X	**Y**	**Z**	**Z+X**	**Z-X**	**Z+Y**	**Z-Y**
0 V	0 V	1 V	-1 V	-1 V	-1 V	-1 V
1 V	1 V	1 V	-2 V	0 V	-2 V	0 V
1 V	1 V	2 V	-3 V	-1 V	-3 V	-1 V
2 V	2 V	1 V	-3 V	1 V	-3 V	1 V

4.3. DAC and ADC Testing

The DAC and ADC were tested in order to make sure that they were operating as they should, but they were not tested with a set of specific input values like the preamplifier or piezo driver. The DAC was tested by sending digital voltages from the Teensy over SPI and the ADC was tested using a few rough inputs from a power supply. With the reference voltage set to 4.7 V, a digital voltage of 0 equals an analog voltage of 0 V and a digital voltage of 255 equals an analog voltage of 4.7 V. To test the DAC, digital voltages were sent from the Teensy ranging from 0–255 in increments of 1, over the course of roughly 2.55 s, using SPI with a speed of 100 Hz. The analog output of the DAC was measured with an oscilloscope and the resulting graph is shown in Figure 30.

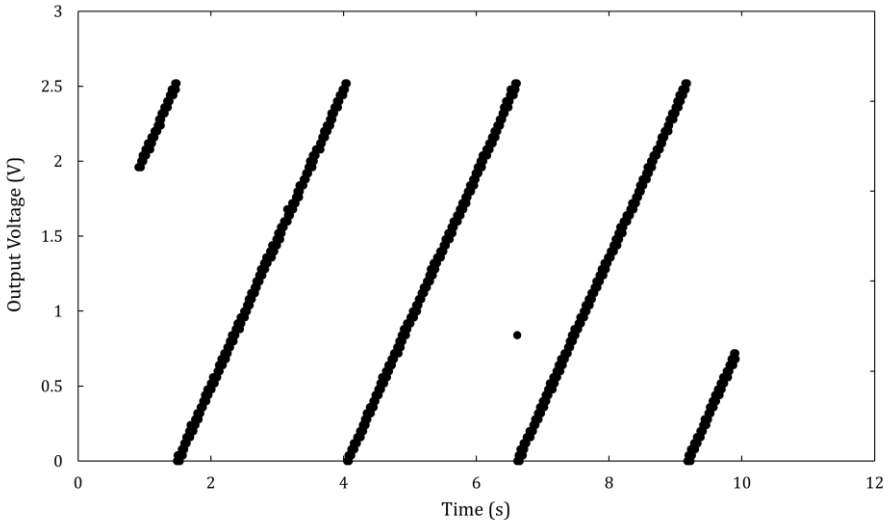

Figure 30. Recreation of oscilloscope graph showing analog output of DAC over time. The input was sent to the DAC by the Teensy and was a range of digital voltages ranging from 0–255, in increments of 1, with a reference voltage of 4.7 V and an SPI speed of 100 Hz. Each set of 255 digital pulses was sent over the course of 2.55 s. This DAC output exactly matches the input provided by the Teensy.

The ADC was tested by supplying the preamplifier input with ~15.4 V from a power supply, meaning that the analog input to the ADC should be ~3.08 V, since the preamplifier divides its input by five, as discussed in Section 4.1. This test was performed with an SPI speed of 8 MHz and a reference voltage of 5 V. The digital output of the ADC was read by the Teensy and plotted using the Arduino serial plotter. The x-axis shows the iteration of the code being run, and the y-axis shows the ADC output for that iteration. The average output of the ADC was 2.6 V $\pm$ 0.5 V, as shown in Figure 31, which corresponds to a theoretical tunneling current of 26 nA $\pm$ 5 nA.

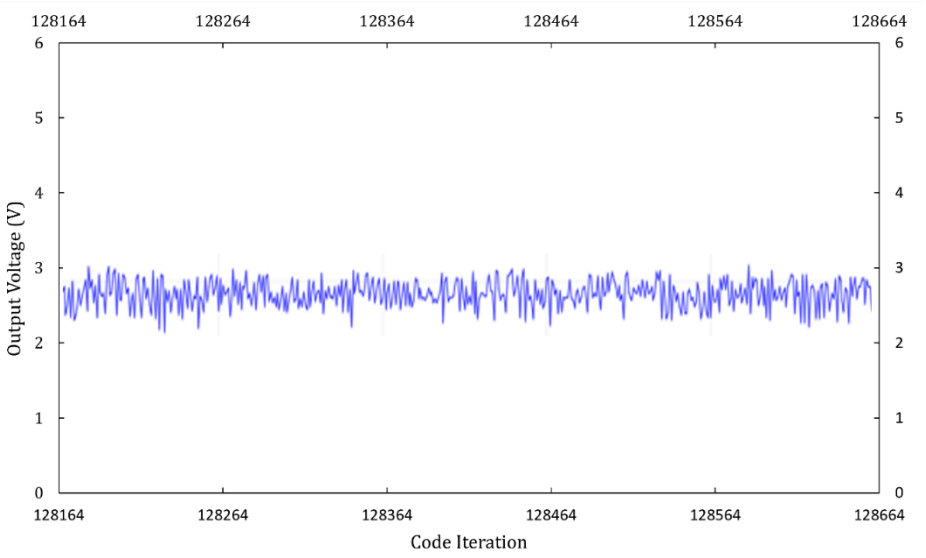

Figure 31. Plot showing the ADC digital output converted to analog by the Teensy. The input to the preamplifier was ~15.4 V, meaning the input to the ADC should have been ~3.08 V. It can be seen from this plot that the average output was less than 3 V, with a noise of ~1 V. The test was performed with an 8 MHz SPI speed and a 5 V reference.

4.4. Piezo Buzzer Testing

After the piezo was cut into quadrants, a multimeter was used to measure the resistance between each quadrant, and it was verified that each quadrant was electrically isolated from one another. To ensure that the ceramic of the piezo was still operational, a function generator was connected to each quadrant and the piezo still operated as normal, as shown by it buzzing most distinctly around its resonant frequency of ~6.5 kHz. Each quadrant was then connected to the function generated individually, and the once again around 6.5 kHz the piezo buzzed the most distinctly. Therefore, it can be said that the electrodes were successfully cut into quadrants while the ceramic remained intact.

Chapter 5

PROGRESS AND PLANS

5.1. Current Status

There are various parts of the STM that have already been completed and some that are currently in progress. Each physical structure of the STM, i.e., the vibration isolation system, scan head and sample stage, have been constructed and assembled in a rough version of their final form. This means that each piece of aluminum has been cut out and has had the proper holes drilled and tapped. The stepper motors have been mounted to the sample stage and the preamplifier has been mounted to the scan head, with a DIP board that connects it and the piezo to the rest of the circuit.

As for the circuit, the stepper motor control has been completed and tested, with all three motors controlled by the Teensy. The circuit for receiving data has been built and data sent by the preamplifier has been read by the Teensy, as described in sections 4.1 and 4.3.

The circuit for sending voltages is still in progress; as of now the Teensy can send voltages to more than one DAC, and the DAC can send voltages to the piezo driver. However, the piezo driver attempts to draw too much current from the DAC, causing a shift down in the voltage. This is being fixed by increasing the total input resistance of the circuit, so it requires less current to operate. Also currently in progress is the mounting of the scanning probe onto the piezo buzzer. A piece of ceramic has been glued to the scanning probe so that it can be electrically isolated from the piezo electrode, but it has not yet been glued to the piezo.

5.2. Future Plans

Future plans for the physical structure of the STM include adjusting the spring length on the vibration isolation system so that each piece sits at the right height and still has a low resonant frequency. In addition to this, magnets need to be added to this system in order to take advantage of eddy current damping to reduce noise. The last structural part to finish is testing the precise movement of the piezo buzzer. Once the sending voltage circuit is

finished and the probe is glued to the piezo, the movement of the piezo in all three dimensions can be tested. Lastly, the main goal for the STM is to obtain a tunneling current between a thin film and the scanning probe. This would be accomplished by utilizing the rough and fine stepper motor approaches discussed above, as well as precise control of the piezo in the z–direction. Once the parts in progress have been completed, this goal of measuring a tunneling current can be accomplished. From that point, a scan could be completed by simply fine tuning each portion and utilizing the x– and y–motion of the piezo.

R e f e r e n c e s

[1] E. Ruska, Nobel Lecture (1986).
[2] H. Busch, Arch. Elektrotechnik **18**, 583-594 (1927).
[3] M. Knoll and E. Ruska, Ann. Physik **12**, 607-640 and 641- 661 (1932).
[4] L. de Broglie, Ann. de Phys. **10**, 22-128 (1925).
[5] L. de Broglie, in *On the Theory of Quanta*, edited by A. F. Kracklauer (AFK, 2004).
[6] M. Knoll and E. Ruska, Z. Physik **78**, 318-339 (1932).
[7] M. Freundlich, Science **142**, 185-188 (1963).
[8] G. Binnig and H. Rohrer, Rev. Mod. Phys. **59**, 615-625 (1987).
[9] G. Binnig, C. W. Quate and Ch. Gerber, Phys. Rev. Lett. **56**, 930-933 (1986).
[10] C. Gorini, R. A. Jalabert, W. Szewc, S. Tomsovic and D. Weinmann, Phys. Rev. B **88**, 035406-18 (2013).
[11] G. Binnig and H. Rohrer, *SCANNING TUNNELING MICROSCOPE*, US Patent 4343993, August 10, 1982.
[12] G. Binnig, H. Rohrer, Ch. Gerber and E. Weibel, Appl. Phys. Lett. **40**, 178-180 (1982).
[13] V. Maurice, W. P. Yang, P. Marcus and J. Electrochem. Soc. **141**, 3016-3027 (1994).
[14] D. M. Kolb, R. Ullmann and T. Will, Science **275**, 1097-1099 (1997).
[15] T. Komeda, Prog. Surf. Sci. **78**, 41-85 (2005).
[16] G. Binnig and H. Rohrer, Surf. Sci. **126**, 236-244 (1983).
[17] D. D. Chambliss, R. J. Wilson and S. Chiang, IBM J. Res. Dev. **39**, 639-654 (1995).
[18] C. Polop, C. Rosiepen, S. Bleikamp, R. Drese, J. Mayer, A. Dimyati and T. Michely, New J. Phys. **74**, 1-19 (2007).
[19] W. Deng, T. Oghi, H. Nejo and D. Fujita, Appl. Phys. A **72**, 595-601 (2001).
[20] J. Malone, B.S. thesis, Houghton University, 2021.
[21] S. Olandt, B.S. thesis, Houghton University, 2019.
[22] S. Daigler, B.S. thesis, Houghton University, 2015.
[23] T. Young, Philos. Trans. Royal Soc. **94**, 1-16 (1804).
[24] M. Plank, *The Theory of Heat Radiation* (P. Blakiston's Son & Co., Philadelphia, 1914).

[25] A. Einstein, Ann. der Phys. **322**, 132-148 (1905).
[26] A. Einstein, in *The Old Quantum Theory*, edited by D. Ter Haar (Pergamon Press Ltd., Oxford, 1967).
[27] C. Jonsson, Am. J. Phys. **42**, 4-11 (1974).
[28] R. B. Dingle, *Asymptotic Expansions: Their Derivation and Interpretation*, (Academic Press, London, 1973).
[29] J. D. Alexander, M. Tortonese and T. Nguyen, *Atomic force microscope with integrated optics for attachment to optical microscope*, US Patent 5952657A, October 14, 1999.